


Review

Hematite: A Good Catalyst for the Thermal Decomposition of Energetic Materials and the Application in Nano-Thermite

Yu Li, Jia Dang, Yuqiang Ma and Haixia Ma * 

Xi'an Key Laboratory of Special Energy Materials/School of Chemical Engineering, Northwest University, Xi'an 710069, China

* Correspondence: mahx@nwu.edu.cn

Abstract: Metal oxides (MOs) are of great importance in catalysts, sensor, capacitor and water treatment. Nano-sized MOs have attracted much more attention because of the unique properties, such as surface effect, small size effect and quantum size effect, etc. Hematite, an especially important additive as combustion catalysts, can greatly speed up the thermal decomposition process of energetic materials (EMs) and enhance the combustion performance of propellants. This review concludes the catalytic effect of hematite with different morphology on some EMs such as ammonium perchlorate (AP), cyclotrimethylenetrinitramine (RDX), cyclotetramethylenete-tranitramine (HMX), etc. The method for enhancing the catalytic effect on EMs using hematite-based materials such as perovskite and spinel ferrite materials, making composites with different carbon materials and assembling super-thermite is concluded and their catalytic effects on EMs is also discussed. Therefore, the provided information is helpful for the design, preparation and application of catalysts for EMs.

Keywords: Fe₂O₃; thermal decomposition; energetic materials; aluminothermic reaction



Citation: Li, Y.; Dang, J.; Ma, Y.; Ma, H. Hematite: A Good Catalyst for the Thermal Decomposition of Energetic Materials and the Application in Nano-Thermite. *Molecules* **2023**, *28*, 2035. <https://doi.org/10.3390/molecules28052035>

Academic Editor: Xiang Zhou

Received: 31 January 2023

Revised: 19 February 2023

Accepted: 20 February 2023

Published: 21 February 2023



Copyright: © 2023 by the authors. Licensee MDPI, Basel, Switzerland. This article is an open access article distributed under the terms and conditions of the Creative Commons Attribution (CC BY) license (<https://creativecommons.org/licenses/by/4.0/>).

1. Introduction

Iron oxide, with the formula Fe₂O₃, has characteristics of abundant natural reserves, non-toxicity, strong corrosion resistance, low preparation cost and excellent visible light absorption ability [1,2]. It usually has four common crystal forms: α -Fe₂O₃ (corundum structure, R3c space group), β -Fe₂O₃ (twin structure, Ia3 space group), γ -Fe₂O₃ (spinel structure, Fd3m space group) and ϵ -Fe₂O₃ (pna 21 space group) [3], which is widely used in optoelectronics [4], gas sensors [5], lithium ion cells and batteries [6], water treatment [7], and solid propellants [8]. Due to the crystal transformation, the structure is different; thus, the application of iron oxide with different crystal form is quite different. Among these crystal forms, hematite (α -Fe₂O₃) is widely used in many fields, such as in Li-ion batteries [6], photoelectrochemical water splitting [9] and as combustion catalysts for solid propellants [10], etc., because of its favorable band position (approximately 2.1 eV), inertness, low toxicity, low cost, and natural abundance.

As many MOs, hematite with a nano size has many different characteristics from the block-sized materials. Researchers carried out many works on the preparation of the nano hematite and obtained many fantastic morphologies including nano-rods, nano-grids, nano-ribbons [11], nano-wires [12], nano-tubes [13], nano-rings [14,15], nano-fibrous [16], hollow spheres [17], etc. Yang et al. [18] directly heated and oxidized iron substrates into ordered α -Fe₂O₃ nano-ribbons and nano-wire arrays in an oxygen atmosphere. Tang and collaborators [19] successfully fabricated porous α -Fe₂O₃ flower-like nanostructures. Gotić et al. [20] successfully achieved the morphological transformation of α -Fe₂O₃ from spindles, pseudo-spheres, nano-tubes to nano-rings by adding divalent metal ions Mn²⁺, Cu²⁺, Zn²⁺, and Ni²⁺ using hydrothermal method. It is found that the introduction of divalent metal cations changes the type of hydroxyl groups on the (001) plane, which makes α -Fe₂O₃ preferentially grow along the c-axis. Lv et al. [21] systematically studied the effect of F⁻ and SCN⁻ on

the growth of α -Fe₂O₃ particles and successfully prepared α -Fe₂O₃ hexagonal nano-rings. The adsorption properties of F[−] on the (100) plane largely slow down its growth along the (100) direction. SCN[−] can induce directional dissolution of α -Fe₂O₃ nanocrystals along the [−221] direction [21,22]. Zhang et al. [23] prepared α -Fe₂O₃ nanocrystals with various morphologies by adjusting the pH value of the K₃[Fe(CN)₆] solution at 140 °C, including snowflake, pair-microplate, dumbbell, cylindrical and spindle three-dimensional structures. Generally speaking, the nano hematite, with different morphology, size and shape, can be achieved by controlling the reaction time, temperature, pH, introducing ligands (such as surfactants, inorganic anions and cations), changing the solvent types (such as common organic solvents, ionic liquids) and other conditions through changing the growth rate of different crystal planes. For further requirement of enhancing application, people also try to make some promotion of hematite, including combining hematite with some carbon materials, making perovskite ferrite, spinel ferrite and super thermites, etc. This paper provides the preparation and application of the hematite-based materials and their catalytic effect for EMs. The effects of the preparation of hematite and ferrite with different morphologies on the thermal decomposition of ammonium perchlorate (AP), cyclotrimethylenetrinitramine (RDX), cyclotetramethylenete-tranitramine (HMX) and other energetic materials (EMs) was studied using thermal analysis technique, and different carbon materials used for preparing composite materials to enhance the catalytic properties of hematite-related materials on EMs were stated. For future application, it is necessary to explore new hematite composited and develop new ideas suitable for industrialization requirements.

2. Preparation of Hematite with Different Morphology and Their Catalytic Effect on EMs

The preparation methods of pure α -Fe₂O₃ mainly include precipitation method, gas phase method, solid phase method, sol-gel method, hydrothermal method, hydrolysis solution, solvothermal method, etc. Usually, the morphologies of hematite prepared by different methods are quite different. The differences in the microscopic structural units manifest anisotropy on the macroscopic scale through thousands of superpositions, and the crystals exhibit different physical and chemical properties in different directions [24–26]. The atomic arrangement and coordination on the surface of nanoparticles determine the properties of nanomaterials, so properties of nanocrystals can be regulated by controlling the morphology [27–30]. Therefore, the methods for synthesizing nano-microcrystals with various geometries and different exposed faces raise much research interest [31–33]. This section covers the synthesis of hematite with different morphologies and their catalytic effects on EMs.

2.1. Preparation of Polyhedral Hematite and the Effect on EMs

The polyhedral structure of α -Fe₂O₃, the most stable iron oxide under environmental conditions, has attracted much attention due to its various potential applications. Lv et al. [34] synthesized well-dispersed single-crystal dodecahedral and octahedral α -Fe₂O₃ particles by a facile hydrothermal method assisted by F[−] anion (the morphology of dodecahedral α -Fe₂O₃ is shown in Figure 1a,b). The dodecahedral particles are hexagonal bipyramid in shape and surrounded by twelve equivalent (101) planes. The only difference between the preparation conditions of dodecahedral and octahedral particles is the concentration of F[−]. Low F[−] concentrations are favorable for the growth of octahedral particles, high F[−] concentration contributes greatly to the growth of dodecahedral particles, while without F[−], the product is quasi-spherical (particle size about 100 nm). If the F[−] concentration exceeds 26.5 mM, the particle size became non-uniform. With a higher F[−] concentration of 28 mM, FeOOH nanorods appeared.

Lv et al. [35] later synthesized dodecahedral α -Fe₂O₃ particles surrounded by twelve (101) faces with the assistance of F[−] and controlled the particle size to be around 150 nm by affecting the nucleation process of α -Fe₂O₃. The thermal behavior using a differential scanning calorimeter (DSC) technique with pure AP and a mixture of AP with 2% α -Fe₂O₃ particles was tested. In the presence of α -Fe₂O₃ dodecahedral nanoparticles, the

LTD (low temperature decomposition peak) at 315 °C almost disappeared, and the HTD (high temperature decomposition peak) shifted to a lower temperature, indicating that the α -Fe₂O₃ dodecahedral nanoparticles can promote the thermal decomposition of AP. The ordinary α -Fe₂O₃ nanoparticles with an average diameter of 100 nm with a similar specific surface area to the synthesized α -Fe₂O₃ dodecahedral nanoparticles was also used to test the thermal decomposition of AP. Comparing curves of b and c, the exposure of the dodecahedral (101) facets was supposed to enhance the catalytic properties of the particles. The curves of b and d indicate that the α -Fe₂O₃ of the same morphology with nano-particles promoted the exothermic heat of AP more than the micro particles. Thus, the exposed facets were supposed to have much influence on the exothermic decomposition of AP.

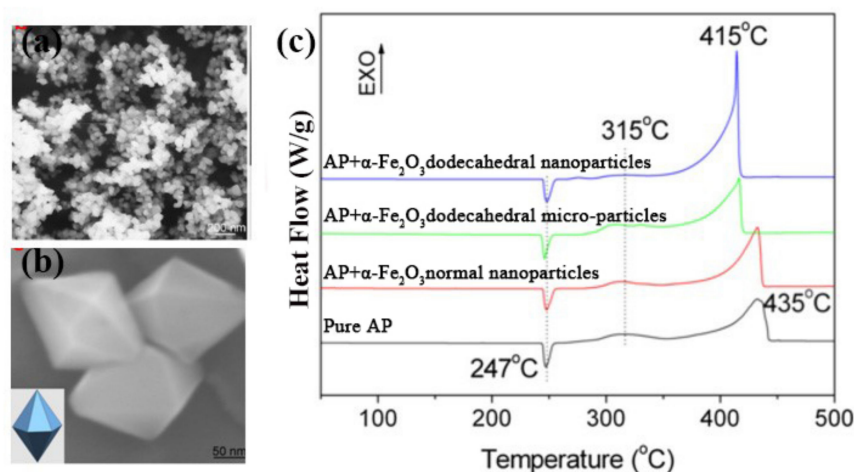


Figure 1. SEM images of (a) synthesized product; The inset of (b) is a geometrical model of the dodecahedral particle; (c) DSC curves for pure AP, AP+ α -Fe₂O₃ dodecahedral nanoparticles, AP+ α -Fe₂O₃ normal nanoparticles, AP+ α -Fe₂O₃ dodecahedral micro-particles. (a–c) Reproduced with the permission of ref. [35]. Copyright 2014, Journal of Nanoparticle Research.

Xu et al. [36] found that the micro-octahedra hematite particles can be obtained using FeCl₃·6H₂O as the precursor, dissolving in aqueous formamide solution by a hydrothermal in a 22 mL Teflon-sealed autoclave and stored at 160 °C for 24 h. While the hematite of monodisperse nanorods can be obtained following the same procedure if the reaction time shortened to 12 h.

The catalytic performance of the obtained different α -Fe₂O₃ on the thermal decomposition of AP was studied by DSC. The DSC curves of AP decomposition with micro-octahedrons, irregular particles and nanorods with different α -Fe₂O₃ samples indicated that all the HTD (436.4 °C) shifted to lower temperatures under the hematite of different morphologies. The prepared α -Fe₂O₃ nanorods exhibited better catalytic activity than the other two samples, and the catalytic performance of irregular particles was slightly better than that of micro-octahedral particles. The authors suggested that the smaller-sized particles may have better performance. Since the three morphologies and sizes in the references are different, we cannot conclude from the above conclusions that the morphology of the nanorods must have a good catalytic effect.

Our group [37] also synthesized well-shaped single-crystal α -Fe₂O₃ particles by a hydrothermal method. The mixture of K₄Fe(CN)₆·3H₂O, sodium carboxymethyl cellulose solution (CMC-Na), poly(vinylpyrrolidone) (PVP), and N₂H₄·H₂O solution were sealed in a 40 mL Teflon-lined autoclave and heated at 200 °C for 6 h to obtain the tetrakaidekahedral hematite.

The structure characterization is shown in Figure 2. The synthesized Fe₂O₃ nanoparticles are uniform in size, and the particle size is 200–250 nm wide and 300–350 nm long. The concentration of K₄Fe(CN)₆·3H₂O was found to have important effect on the formation of

morphology. When the used $K_4Fe(CN)_6 \cdot 3H_2O$ is 0.2 mmol, the oblique parallelepiped iron oxide was obtained.

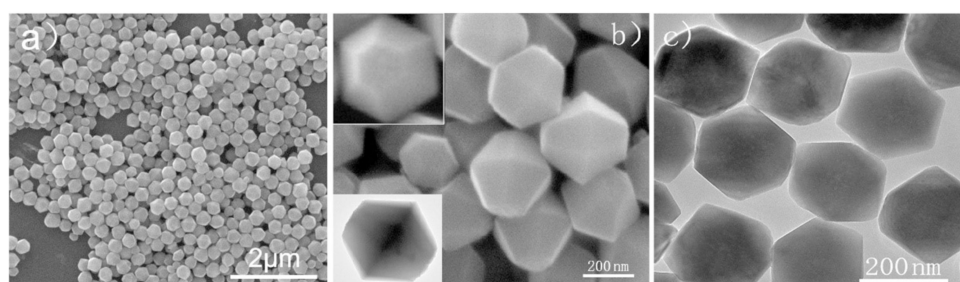


Figure 2. The tetrakaidekahedral $\alpha\text{-Fe}_2\text{O}_3$ nanocrystals synthesized at 200 °C for 6 h. (a,b) Low- and high-magnification SEM image of tetrakaidekahedral $\alpha\text{-Fe}_2\text{O}_3$ crystals. Insets (top left and bottom left) represents the cross-section of the as-prepared product and HRTEM images of a single tetrakaidekahedral crystal; (c) TEM image of the tetrakaidekahedral $\alpha\text{-Fe}_2\text{O}_3$ crystals. (a–c) Reproduced with the permission of ref. [37]. Copyright 2011, Inorganic Chemistry.

Further study [38] about the catalytic effect of the tetrakaidekahedral hematite compared to the grainy hematite on the thermal decomposition of hexanitrohexaazaisowurtzitan (HNIW, CL-20) indicates that the exothermic peak temperatures of CL-20 with tetrakaidekahedral- Fe_2O_3 and grainy- Fe_2O_3 decreased by 5.53 and 4.95 K, respectively (Figure 3). Further non-isothermal thermal decomposition kinetic studying indicated that the tetrakaidekahedral nano- Fe_2O_3 did not change the thermal decomposition mechanism of CL-20, while the grainy nano- Fe_2O_3 changed the thermal decomposition mechanism of CL-20. From the decrease in the thermal decomposition peak temperature and the corresponding kinetic evaluation, the tetrakaidekahedral nano- Fe_2O_3 exhibits better catalytic activity on CL-20 than the grainy nano- Fe_2O_3 .

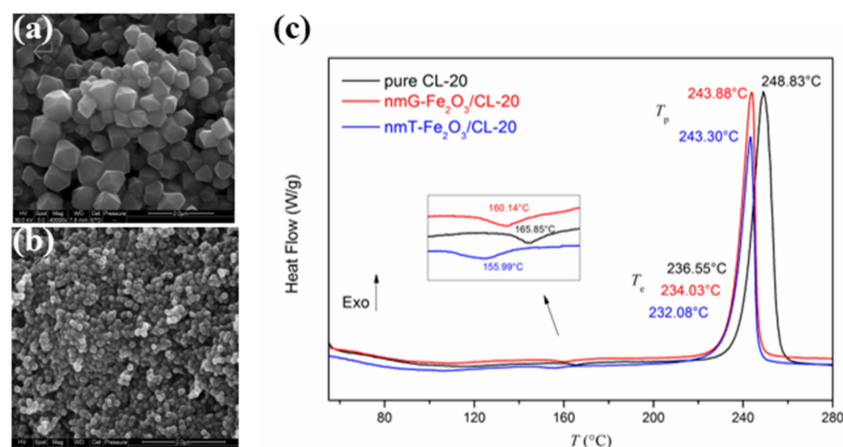


Figure 3. SEM images of the two nano- Fe_2O_3 with a resolution of 2 μm . (a) tetrakaidekahedral- Fe_2O_3 (nmT- Fe_2O_3), (b) grainy- Fe_2O_3 (nmG- Fe_2O_3) and DSC curves of CL-20, nmT- $\text{Fe}_2\text{O}_3/\text{CL-20}$ and nmG- $\text{Fe}_2\text{O}_3/\text{CL-20}$ at a heating rate of 10 $\text{K}\cdot\text{min}^{-1}$ (c). (a–c) Reproduced with the permission of ref. [38]. Copyright 2016, Propellants Explosives Pyrotechnics.

2.2. Preparation of Granular Hematite and the Effect on EMs

To study the effect of different iron precursors on the particle size of hematite and its effect on nitrocellulose (NC), Benhammada et al. [39]. successfully prepared $\alpha\text{-Fe}_2\text{O}_3$ nanoparticles by a simple and direct hydrothermal method using three different precursors (FeCl_3 , $\text{Fe}(\text{NO}_3)_3$ and $\text{Fe}(\text{SO}_4)_2$). In brief, a stoichiometric amount of iron precursor was dissolved in distilled water under stirring and the solution of ammonia (34%) was used to adjust $\text{pH} = 8$, then in an autoclave and heated at 180 °C for 24 h. The spherical

nanoparticles with 110 ± 9 , 90 ± 6 and 80 ± 7 nm corresponding to FeCl_3 , $\text{Fe}(\text{NO}_3)_3$ and $\text{Fe}(\text{SO}_4)_2$, respectively, were obtained. The catalytic activity of the as-prepared nanoparticles for the thermal decomposition of NC was investigated by DSC. All curves show only one exothermic peak, corresponding to the breaking of the O- NO_2 bond.

The as-synthesized nanocatalysts with different sizes have a slight effect on the peak decomposition temperature of NC, while the activation energy is apparently reduced. The Fe_2O_3 prepared using ferric chloride as a precursor has the greatest catalytic effect on NC.

Our group [39,40] successfully prepared granular nanoscale α - Fe_2O_3 particles by a simple hydrothermal method using $\text{FeCl}_3 \cdot 6\text{H}_2\text{O}$, urea, glycine in distilled water at 160°C for 10 h. The SEM and TEM images of the prepared granular α - Fe_2O_3 nanoparticles with a small average particle size of 210 nm are shown in Figure 4a,b.

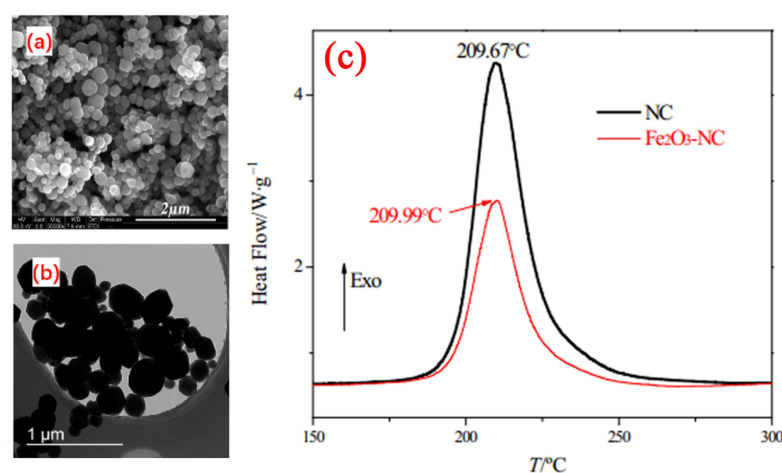


Figure 4. SEM (a), Low-magnification TEM (b) micrographs of α - Fe_2O_3 nanoparticles and DSC curves of NC and Fe_2O_3 -NC (c) obtained at a heating rate of $10^\circ\text{C min}^{-1}$. (a–c) Reproduced with the permission of ref. [40]. Copyright 2016, Journal of Analytical and Applied Pyrolysis.

The catalytic effect of granular nanoscale hematite was studied by DSC technique. The obtained DSC curves are shown in Figure 4c. The thermal decomposition peak of α - Fe_2O_3 /NC composites was almost equal with NC, but the activation energy (E_a) of the composite decreased by $15.37 \text{ kJ}\cdot\text{mol}^{-1}$. Further detailed thermal decomposition mechanism about the composites and NC suggested that the O- NO_2 bond cleavage, the condensed-phase decomposition and even the reaction of NO_2 and HCHO gases were promoted by the as-prepared α - Fe_2O_3 . The hematite nanoparticles were supposed to promote the O- NO_2 bond cleavage, the condensed-phase decomposition and the reaction of NO_2 and HCHO gases, thus, accelerate the thermal decomposition reaction rate of NC.

Elbasuney et al. [41] prepared high crystalline, monodisperse Fe_2O_3 nanoparticles with an average particle size of 3.39 nm using a hydrothermal method, then the obtained Fe_2O_3 was integrated into HMX by a co-precipitation technique. The effect of Fe_2O_3 (1 wt%) on the pyrolysis of HMX was investigated using DSC. The main exothermic decomposition peak of HMX decreased from 285°C to 272°C and the decomposition enthalpy increased from $1016 \text{ J}\cdot\text{g}^{-1}$ to $1750 \text{ J}\cdot\text{g}^{-1}$. Mechanistic analysis revealed that Fe_2O_3 can convert HMX pyrolysis from C-N cleavage to hydrogen atom abstraction by releasing active surface OH radicals. Furthermore, the released NO_2 and CH_2O can be adsorbed on the nanocatalyst surface, providing high decomposition enthalpy.

2.3. Preparation of Rod-Shaped Hematite and the Effect on EMs

The heat treatment temperature always affects the phase transition process of amorphous δ - FeOOH . Zhang et al. [42] prepared α - FeOOH nanorods by hydrothermal reaction at 100°C for 6 h using $\text{Fe}(\text{NO}_3)_3 \cdot 9\text{H}_2\text{O}$ and KOH as raw materials. Different porous single crystal α - Fe_2O_3 nanorods were obtained after the samples were heat-treated at 300, 350, 450

and 600 °C. The catalytic effect of the prepared nano-rod samples on AP was investigated by differential temperature analysis (DTA). The α -Fe₂O₃ nanorods obtained by heat treatment at 350 °C was proved to reduce the pyrolysis temperature of AP by 71.4 °C.

To gain insight into the intrinsic function of catalysts in AP decomposition and guide the design of catalysts. Zhou et al. [43] proposed a new method to quantitatively evaluate the catalytic ability of MOs for AP. Two metrics, intrinsic peak temperature (T_{HTD}^*) and catalytic density (ρ_T^*), are introduced during pyrolysis to decouple the activity and the number of catalyst sites. Hematite nanostructures with different shapes were used as model catalysts to verify the feasibility of this method. The different morphology of Fe₂O₃ was obtained using different precursors and different preparation methods. Rod-like Fe₂O₃ NPs were obtained using Fe(NO₃)₃ and NaOH as the precursors, after being sealed in the Teflon reactor at 180 °C for 40 min and calcined at a tube furnace at 350 °C for 4 h. The rhombic Fe₂O₃ NPs were obtained using FeCl₃ and urea as precursors, after the solution was refluxing at 95 °C for 4 h and calcined at a tube furnace at 500 °C for 3 h. The pseudo-cubic Fe₂O₃ NPs were obtained using Fe(NO₃)₃·9H₂O and PVP by hydrothermal method at 180 °C for 3 h and annealing at 600 °C for 90 s. The AP decomposition HTD by DSC of 2 wt% ro-Fe₂O₃, rh-Fe₂O₃ and pc-Fe₂O₃ were 358.1, 381.5 and 395.0 °C, respectively, which were 76.8, 53.4 and 39.9 °C lower than that of pure AP decomposition (434.9 °C). The rod-like α -Fe₂O₃ exhibited the best catalytic performance for the thermal decomposition of AP, with the lowest T_{HTD}^* of 345.1 °C and the highest ρ_T^* of 0.544, which implies the highest number and activity of catalytic sites.

2.4. Preparation of Hematite with Other Morphologies and the Effect on EMs

As an important environmentally friendly MOs, in addition to the common morphology, hematite nanostructures with various shapes have also attracted extensive attention to meet better requirements.

Nano-disc morphology: Shi et al. [44] successfully synthesized hematite hexagonal nano-discs with dominant (001) and lateral (110) planes by introducing ethylene glycol (EG) into a hydrothermal system. The results show that the proper addition of EG in the hydrothermal system creates equilibrium conditions for the nucleation and growth of crystals, resulting in the formation of uniform α -Fe₂O₃ hexagonal nano-discs with major (001) crystal planes.

The DTA curves of AP and AP-based composites samples indicated that the α -Fe₂O₃ hexagonal nano-discs exhibited superior catalytic performance compared with the α -Fe₂O₃ irregular particles. Under the action of α -Fe₂O₃ hexagonal nano-discs, the exothermic peak induced by the pyrolysis of AP [36] were shifted from 516.6 °C to lower temperatures of 356.0 °C and 394.0 °C. While α -Fe₂O₃ irregular particles only induce a decrease from 516.6 °C to 419.8 °C. The two shifts to lower peak temperature can be attributed to the different catalytic active lattice and composition of the exposed (001) and (110) crystalline planes due to their different planes.

Hexagonal cone (HC) morphology: Sharma et al. [45] developed a facile and environmentally friendly method for the synthesis of α -Fe₂O₃ in the HC form by adding neem leaf extract to an aqueous solution of ferric chloride. The morphology and microstructure of the synthesized α -Fe₂O₃ HCs were investigated by Field Emission SEM (FESEM) measurement, as shown in Figure 5. The nanostructures are hexagonal pyramid shaped with an average diameter of 400–500 nm. Then, the synthesized α -Fe₂O₃ HCs were used as burn rate enhancers for thermal decomposition of AP and combustion of composite solid propellant. From the thermal analysis (Figure 6), the addition of the synthesized α -Fe₂O₃ HCs significantly decreased the decomposition temperature of AP by 75 °C, indicating that the green synthesized α -Fe₂O₃ HCs have an effective catalytic effect on the thermal decomposition of AP. The α -Fe₂O₃ HCs can simultaneously accelerate LTD and HTD. Further kinetic studies show that the E_a^* value for the ignition is much lower, which is due to the efficient adsorption of gaseous products on the green-synthesized α -Fe₂O₃ HCs during the dissociation of AP, and thus α -Fe₂O₃ HCs significantly promotes the gaseous reaction.

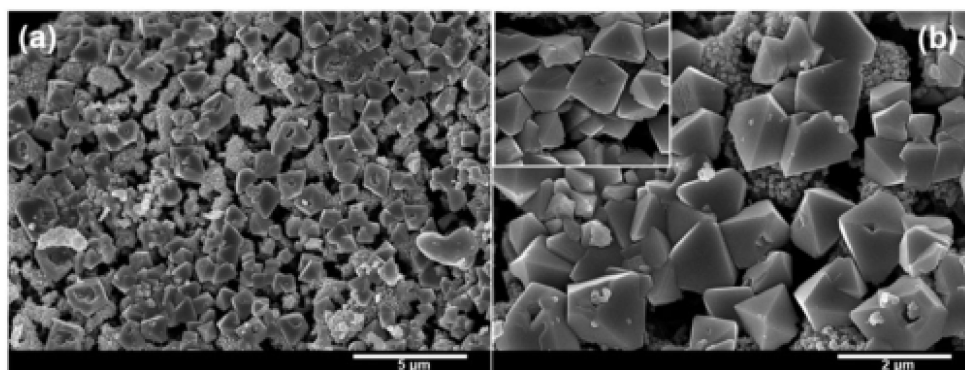


Figure 5. FESEM images at low (a) and high (b) magnification of the synthesized Fe_2O_3 hexagonal cones. (a,b) Reproduced with the permission of ref. [45]. Copyright 2015, New Journal of Chemistry.

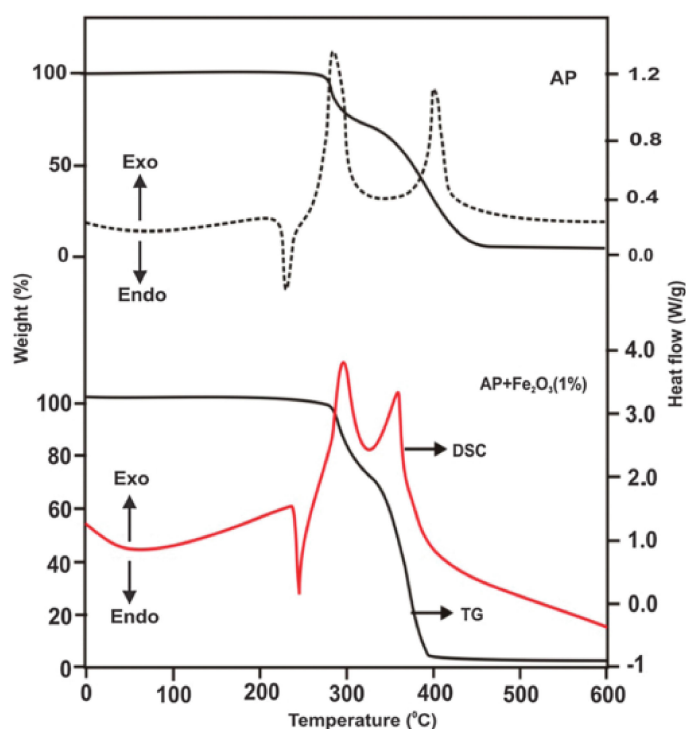


Figure 6. TG-DSC curves of pure AP and AP with the green synthesized Fe_2O_3 hexagonal cones (1 wt%). Reproduced with the permission of ref. [45]. Copyright 2015, New Journal of Chemistry.

For reactive precipitations, they are usually fast or transient reaction processes, with nucleation induction periods typically around 1 ms. The rate of nucleation and crystal growth depends largely on the supersaturation of the reaction environment. Cao et al. [46] heated $\text{FeCl}_3 \cdot 6\text{H}_2\text{O}$ and urea aqueous solution at 95°C in two different tanks. Then, the two solutions were sprayed into the packing of a rotating packed bed (RPB) to get red precipitate. After transferred into a thermostat bath, the reaction was kept going at 95°C for 4 h under stirring and refluxing. Finally, the red product was obtained after the red precipitate cake was filtered, washed and calcined in ambient atmosphere at 500°C for 3 h and drying. When the high gravity level (G , the ratio of centrifugal acceleration generated by the rotating packing to the local gravity acceleration) of the RPB reactor equals 68, the uniform rhombohedral sphere can be formed. The DSC results indicated that the addition of 2 wt% of 84 nm $\alpha\text{-Fe}_2\text{O}_3$ can decrease the LTD and HTD temperatures of AP by 14.4°C and 53.4°C , respectively, and increase the heat released from AP from $864 \text{ J} \cdot \text{g}^{-1}$ to $1235 \text{ J} \cdot \text{g}^{-1}$.

Table 1 summarizes the preparation methods, thermal decomposition temperature (T_p), reaction heat (ΔH), and apparent activation energy (E) of these hematite with energetic composites of different morphologies reported in recent years. The morphologies and particle sizes have a great influence on the thermal decomposition process of EMs. from the decrease in the decomposition temperature and activation energy.

Table 1. Summary of thermal behavior parameters of EMs with different morphologies of hematite.

Morphologies	Samples	Preparation Method	Mass Ratios	T_p	ΔH	E	Refs.
dodecahedral	AP	assistance of F^-	0	435.0	-	-	[35]
	Fe_2O_3/AP		2%	415.0	-	-	
nanorods	AP	one-pot	0	436.4	-	-	[36]
	Fe_2O_3/AP		1%	387.5	-	-	
micro-octahedrons	Fe_2O_3/AP	hydrothermal	1%	426.4	-	-	
	CL-20		0	248.8	-	181.1	[38]
tetrakaidecahedral grainy	$Fe_2O_3/CL-20$	hydrothermal	33.33%	243.3	-	177.8	
	$Fe_2O_3/CL-20$		33.33%	243.9	-	176.1	
granular	NC	hydrothermal	0	208.6	-	$(17 \pm 2) \times 10 + 01$	[39]
	$Fe_2O_3/NC/Cl$		5%	209.2	-	$(16 \pm 2) \times 10 + 01$	
	$Fe_2O_3/NC/N$		5%	209.4	-	$(17 \pm 3) \times 10 + 01$	
	$Fe_2O_3/NC/S$		5%	209.1	-	$(17 \pm 1) \times 10 + 01$	
granular	NC	hydrothermal	0	209.6	-	-	[40]
	Fe_2O_3/NC		12.6%	209.9	-	189.9	
granular	HMX	co-precipitation	0	285.0	-	-	[41]
	Fe_2O_3/HMX		1%	272.0	-	-	
nano-rods	AP	hydrothermal	0	428.5	-	-	[42]
	Fe_2O_3/AP		2%	351.7	-	-	
rod-like	AP	hydrothermal	0	434.9	-	245.8 ± 32.4	[43]
	ro- Fe_2O_3/AP		2%	358.1	1517.4	133.6 ± 6.3	
rhombic	rh- Fe_2O_3/AP	hydrothermal	2%	381.5	1494.8	153.0 ± 8.7	
	pc- Fe_2O_3/AP		2%	395.0	1469.1	161.2 ± 0.5	
pseudo-cubic	AP	hydrothermal	0	516.6	-	-	[44]
	Fe_2O_3/AP		1%	394.0	-	-	
nano-disks irregular particles	Fe_2O_3/AP	hydrothermal	1%	419.8	-	-	
	AP		0	445.0	-	160.0 ± 2.0	[45]
hexagonal cone	AP	indica (neem) leaf extract.	0	445.0	-	160.0 ± 2.0	[45]
	Fe_2O_3/AP		1%	370.0	-	112.0 ± 5.0	
rhombohedron	AP	high-gravity reactive precipitation	0	437.4	860.0	218.0	[46]
	G30 Fe_2O_3/AP		2%	396.7	984.0	167.1	
	G220 Fe_2O_3/AP		2%	384.0	1235.0	163.3	

Note: T ($^{\circ}C$); ΔH ($J \cdot g^{-1}$); E ($KJ \cdot mol^{-1}$).

3. The Preparation of Ferrite and the Application on the EMs

3.1. Perovskite Ferrite

Perovskite type of metal oxides, with the general formula of ABO_3 [47], are compounds composed of two or more simple oxides with high melting points. The structure is shown in Figure 7 ("A" is an alkaline-earth metal, "B" is a transition metal, red sphere represent oxygen atoms), A site is usually an alkaline earth metal or rare earth metal cations, and B position is always transition metal cations. It can be partially substituted by other metal cations with similar radii to keep its crystal structure basically unchanged [48]. Tanaka et al. [49] proposed the main strategies of designing this kind of materials as follows: (1) select the B site element that mainly determines the catalytic activity; (2) control the valence and vacancy by selecting the A site element, including partial substitution; (3) The synergistic effect of the constituent elements is mainly the B site transition elements; (4) enlarge the specific surface area by forming small particles or dispersing on the carrier; (5) add precious metals and their proper regeneration to achieve highly active catalysts. The preparation of pure perovskite oxides or the integration of MOs requires long-term

high temperature calcination ($>800\text{ }^{\circ}\text{C}$), which results in a small specific surface area [50], and when used as a catalyst, only the outer surface is accessible. The introduction of porous structure will always increase the specific surface area of the material, thereby improving the catalytic performance. Since the catalytic activity is closely related to the surface properties of the material, the specificity of the perovskite structure makes it widely used in catalysis. Therefore, its application potential in solid propellants has also attracted attention.

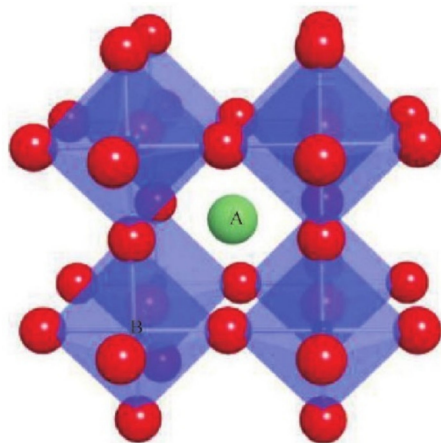


Figure 7. Perovskite crystal structure. Reproduced with the permission of ref. [47]. Copyright 2021, Chemical Industry and Engineering Progress.

Lanthanum ferrite (LaFeO_3), a perovskite (ABO_3) structure, has received extensive attention for its advantages such as stable framework structure and chemical stability [51]. Compared with single MOs, the special perovskite structure has more lattice distortions and vacancies [52].

Thirumalairajan et al. [53] synthesized the well-organized spherical LaFeO_3 microspheres with an average diameter of 2–4 μm by a self-assembly process controlled synthesis using $\text{La}(\text{NO}_3)_3 \cdot 6\text{H}_2\text{O}$, $\text{Fe}(\text{NO}_3)_3 \cdot 6\text{H}_2\text{O}$ and $\text{C}_6\text{H}_8\text{O}_7 \cdot \text{H}_2\text{O}$ as starting materials.

The perovskite LaFeO_3 nano-particles are able to catalyze the reaction between CO and NO_x in vehicle emissions [54,55]. It is also worth noting that CO and NO_x are the two main products of the thermal decomposition of HMX. The pressure exponent would decrease if the propellant for the reaction between CO and NO_x could be catalyzed on the combustion surface of nitrate plasticized polyether (NEPE) [56]. Therefore, perovskite-type oxides such as LaFeO_3 are expected to be used as novel catalysts or modifiers for NEPE propellants.

Later, Wei et al. [57] used a novel stearic acid solution combustion method to directly prepare perovskite LaFeO_3 and $\alpha\text{-Fe}_2\text{O}_3$ with high specific surface area under the appropriate stearic acid-nitrate ratio of 1:1. The catalytic activity of the perovskite LaFeO_3 and $\alpha\text{-Fe}_2\text{O}_3$ for thermal decomposition of HMX was investigated by TG and TG-EGA techniques. The experimental results show that the catalytic activity of perovskite LaFeO_3 is much higher than that of $\alpha\text{-Fe}_2\text{O}_3$, which is due to the higher concentration of surface adsorbed oxygen (Oad) and hydroxyl groups of LaFeO_3 .

For solid propellants, Wei [57] and Wang [58] conducted a simple study on the application of LaFeO_3 catalysts, but serious sintering problems occurred during the preparation of LaFeO_3 , which hindered the dispersion of LaFeO_3 particles in the propellant matrix. Our group [59] prepared the spherical LaFeO_3 with uniform particle size and good dispersion by solvothermal and post-heat treatment. However, due to the large particle size and low specific surface area of LaFeO_3 , its catalytic activity is limited to a certain extent. To improve its catalytic activity, a 3D core-shell heterostructure $\text{LaFeO}_3@\text{MnO}_2$ composite was constructed. The synthesis route is shown in Figure 8. The catalytic effect on different EMs of the prepared samples was studied by DSC, the curves are shown in Figure 9. Under the effect of $\text{LaFeO}_3@\text{MnO}_2$, the decomposition temperature of AP decreased from $403.73\text{ }^{\circ}\text{C}$ to $281.38\text{ }^{\circ}\text{C}$, the energy release increased to $966.5\text{ J}\cdot\text{g}^{-1}$ from $649.6\text{ J}\cdot\text{g}^{-1}$, and the apparent

activation energy of AP decreased from $139.05 \text{ kJ}\cdot\text{mol}^{-1}$ to $110.88 \text{ kJ}\cdot\text{mol}^{-1}$. In addition, $\text{LaFeO}_3\text{@MnO}_2$ also showed efficient catalysis for the thermal decomposition of CL-20 and HMX. The enhanced catalytic activity is attributed to the unique core-shell heterostructure and the synergistic effect between the LaFeO_3 core and the ultrathin MnO_2 shell.

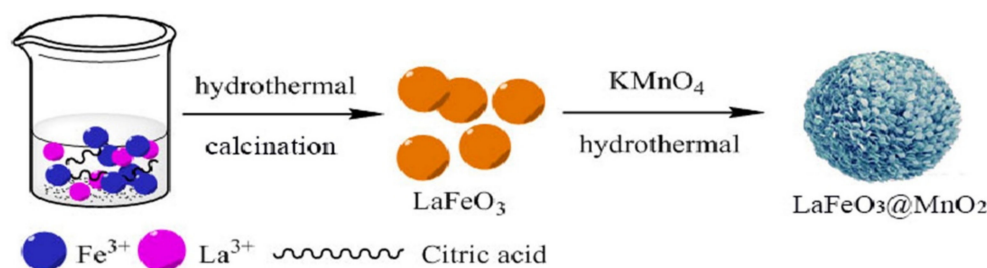


Figure 8. Synthetic routes of LaFeO_3 and $\text{LaFeO}_3\text{@MnO}_2$. Reproduced with the permission of ref. [59]. Copyright 2020, Advanced Powder Technology.

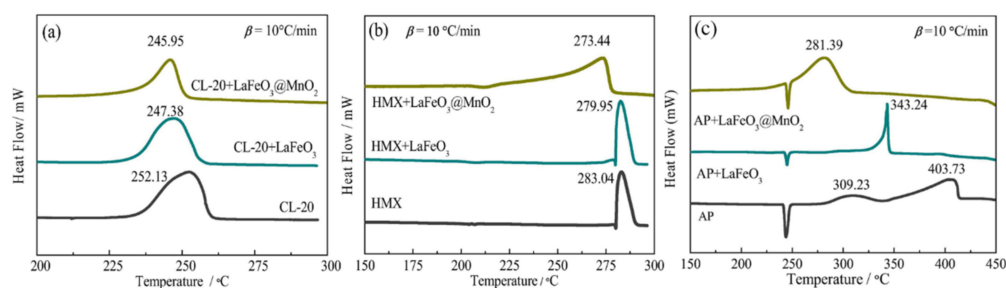


Figure 9. DSC curves for (a) CL-20 and (b) HMX (c) AP with different catalysts. (a–c) Reproduced with the permission of ref. [59]. Copyright 2020, Advanced Powder Technology.

3.2. Spinel Ferrite

Fe_2O_3 , Fe_3O_4 with micro-nano structure and general ferrite compounds such as $\text{MOs}\cdot\text{Fe}_2\text{O}_3$, $\text{M}^{\text{II}}\text{Fe}^{\text{III}}_2\text{O}_4$ and MFe_2O_4 (M is Mn, Co, Fe, Ni, Cu, etc.) play an important role in clean energy, green science and dealing with environmental pollution problems [60–67]. MOs containing iron, cobalt, and nickel elements usually have a spinel structure. The spinel-structure materials have special properties such as strong magnetic properties, high resistivity, high temperature resistance, and low preparation costs, which are widely used in magnetic recording materials, giant magnetic materials, microwave absorbing materials, etc. [68]. In addition, bimetallic oxides generally have better catalytic activity for the thermal decomposition of oxidants [69–71]. Several bimetallic iron oxides have been fabricated and used for thermal decomposition of AP [72–78]. These studies confirmed the catalytic activity of ferrate for the thermal decomposition of AP. However, due to the different APs that were used, the preparation method and the added amount of ferrate were quite different, it is hard to evaluate the catalytic performance of different ferrates based on data from different literatures. Therefore, we just list the data in Table 2.

Zhang et al. [79] investigated the catalytic effect of different ferrates on the thermal decomposition of AP. As shown in Figure 10, three ferrates (NiFe_2O_4 , ZnFe_2O_4 , and CoFe_2O_4) were prepared by a facile solvothermal method. The NiFe_2O_4 , CoFe_2O_4 and ZnFe_2O_4 particles have hollow structures with average particle sizes of 70, 220 and 360 nm, respectively. The catalytic performance of ferrate on the thermal decomposition of AP was studied by DSC and TG-DTG methods, the corresponding curves are shown in Figure 11. The result indicated that CoFe_2O_4 had the best catalytic activity, which can decrease the T_{HTD} and E_a of AP by 108.99°C and $37.38 \text{ kJ}\cdot\text{mol}^{-1}$, respectively. Further thermal analysis shows that the addition of ferrate had no obvious effect on the gas phase decomposition products of AP but had a greater impact on the energy barrier of AP pyrolysis. The excellent

catalytic activity of CoFe_2O_4 is supposed to be attributed to the synergistic effect between Fe and Co.

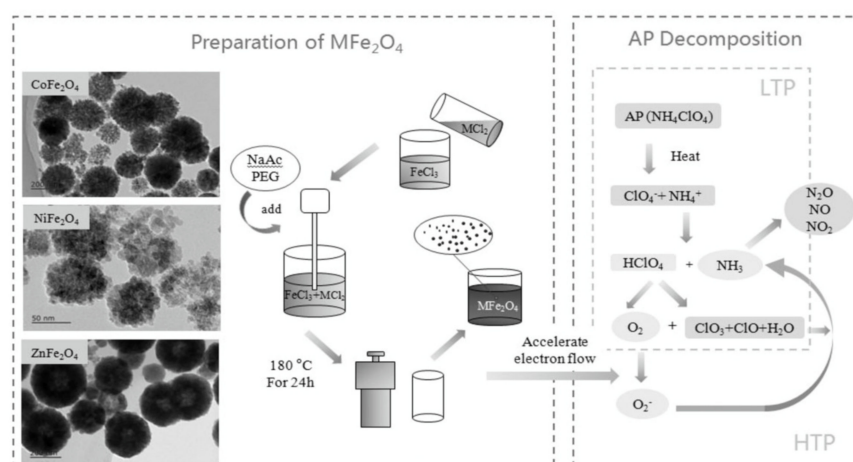


Figure 10. Illustration of ferrate fabrication and the catalytic mechanism for thermal decomposition of AP. Reproduced with the permission of ref. [79]. Copyright 2020, Propellants Explosives Pyrotechnics.

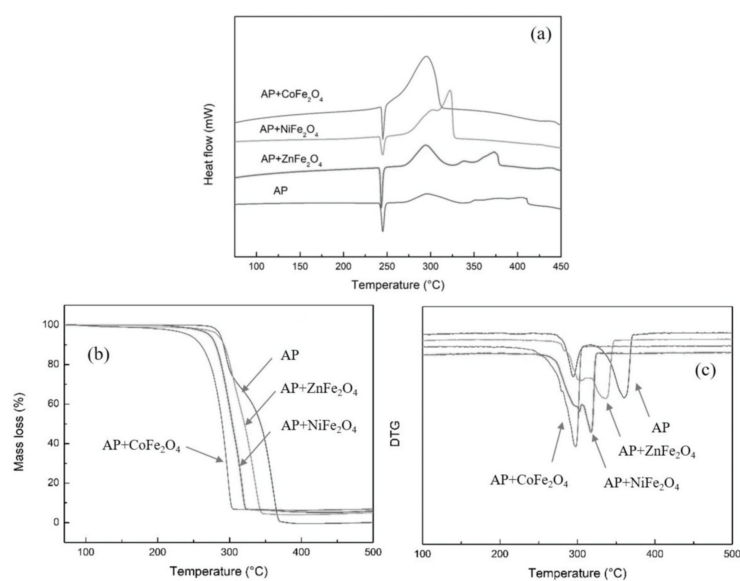


Figure 11. DSC and TG-DTG curves of AP before and after mixed with different ferrates at $10\text{ }^\circ\text{C min}^{-1}$ (a) DSC curves, (b) TG curves, (c) DTG curves. (a–c) Reproduced with the permission of ref. [79]. Copyright 2020, Propellants Explosives Pyrotechnics.

To further enhance the effect, some preparation methods for enlarging the specific surface area were adopted. Xiong et al. [73] prepared nano CoFe_2O_4 with three-dimensional porous structure by a colloidal crystal template method using $\text{Co}(\text{NO}_3)_2 \cdot 6\text{H}_2\text{O}$ and $\text{Fe}(\text{NO}_3)_3 \cdot 9\text{H}_2\text{O}$ as the precursors. The prepared porous nano CoFe_2O_4 particles have a typical spinel structure with a pore size of about 200 nm (Figure 12). The specific surface area is significantly higher than that of 40 nm spherical CoFe_2O_4 , reaching $55.646\text{ m}^2 \cdot \text{g}^{-1}$. The catalytic effects of porous nano CoFe_2O_4 and spherical nano CoFe_2O_4 on the thermal decomposition performance of AP were comparatively studied by DSC, and the DSC curves are shown in Figure 13. The porous nano CoFe_2O_4 with content of 6% can significantly reduce the HTD of AP by up to $91.46\text{ }^\circ\text{C}$. Moreover, the porous CoFe_2O_4 with only 2% can increase the decomposition reaction heat up to $1120.88\text{ J} \cdot \text{g}^{-1}$, which is 2.3 times that of pure AP. The thermal decomposition mechanism of AP catalyzed by porous CoFe_2O_4 was explored. Due to the high specific surface area ($55.646\text{ m}^2 \cdot \text{g}^{-1}$) and high adsorption capacity of

porous nanocomposite MOs, the formed gaseous intermediate products are adsorbed on the surface of porous nanocomposite CoFe_2O_4 (as shown in Figure 14). Then, the gaseous intermediate products are desorbed after electron transfer on the active site and separated from the pore wall to generate final products such as HCl , H_2O , Cl_2 , O_2 , NO , N_2O , and NO_2 [80].

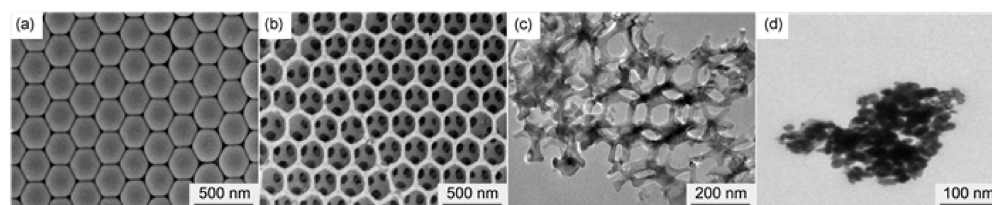


Figure 12. SEM image of (a) colloidal crystal template of polystyrene (PS); (b) SEM image of nanoporous CoFe_2O_4 ; (c) TEM image of nanoporous CoFe_2O_4 ; (d) TEM image of nanospheres CoFe_2O_4 . (a–d) Reproduced with the permission of ref. [73]. Copyright 2016, Acta Physico-Chimica Sinica.

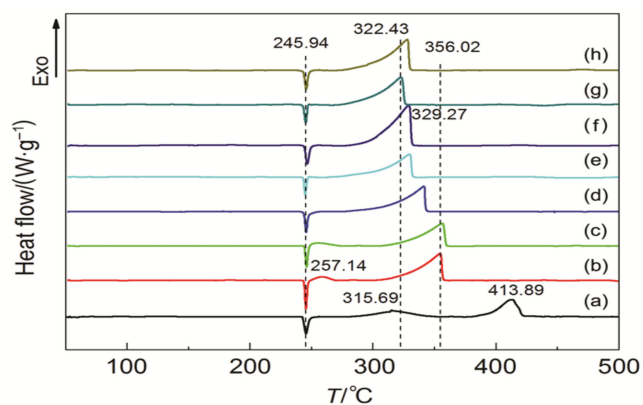


Figure 13. DSC curves of the AP decomposition in the absence and presence of different blend ratios of nanoporous CoFe_2O_4 . Reproduced with the permission of ref. [73]. Copyright 2016, Acta Physico-Chimica Sinica. (a) pure AP; (b) AP + nanoporous CoFe_2O_4 -1% (ω); (c) AP + nanoporous CoFe_2O_4 -2%; (d) AP + nanoporous CoFe_2O_4 -3%; (e) AP + nanoporous CoFe_2O_4 -4%; (f) AP + nanoporous CoFe_2O_4 -5%; (g) AP + nanoporous CoFe_2O_4 -6%; (h) AP + nanoporous CoFe_2O_4 -7%.

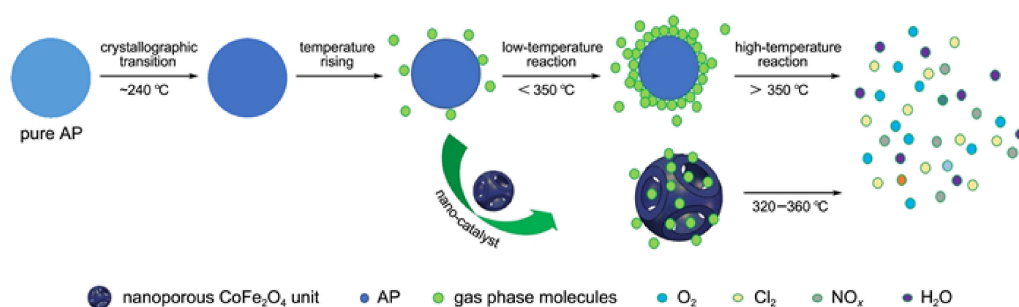


Figure 14. Schematic diagram of the thermal AP decomposition process in the absence and presence of nanoporous CoFe_2O_4 . Reproduced with the permission of ref. [73]. Copyright 2016, Acta Physico-Chimica Sinica.

Wang et al. [81] used nickel nitrate, ferric nitrate, and cerium nitrate as oxidants, water-soluble hydrazine fuels as reducing agents, and added metal cation complexing agents and dispersants to prepare well dispersed Ce-doped nano NiFe_2O_4 by sol combustion synthesis method. The prepared nano powder has a particle size range of 30–60 nm, good dispersibility, and the Ce doping content is within 0.09 (as shown in Figure 15a). The

catalytic effect of the product on the thermal decomposition of AP was studied by DSC (as show in Figure 15b). The results show that with the increase in Ce doping amount, the nano particles make the HTD of AP gradually decrease, and the apparent decomposition heat increases. When the Ce doping amount is 0.09, the HTD of AP is reduced by 57.8 °C.

Table 2 summarizes the related preparation methods of the perovskite and spinel ferrite as well as their catalytic effect to EMs thermal parameters in recent years. The catalytic effect of the ferrites is usually better than the corresponding MOs with single metal cation due to the synergistic effect of the bimetal.

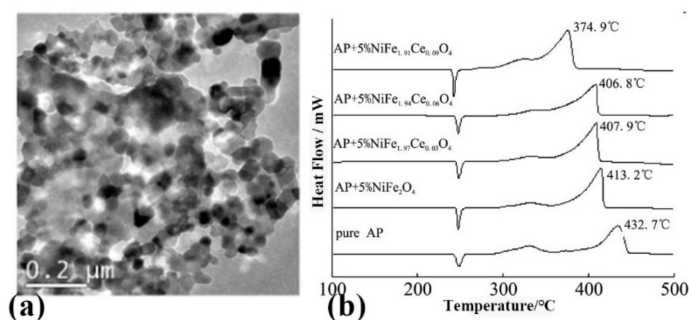


Figure 15. TEM images of the samples (a); DSC curves of different samples (b). Reproduced with the permission of ref. [81]. Copyright 2012, Journal of Solid Rocket Technology.

Table 2. Summary of thermal behavior parameters of different ferrite EMs composites.

Materials	Samples	Preparation Method	Mass Ratios	T_p	ΔH	E	Refs.
ABO ₃	AP	solvothermal and post-heat treatment	0	403.7	-	139.1	[59]
	LaFeO ₃ /AP		20%	343.2	-	126.5	
	LaFeO ₃ @MnO ₂ /AP		20%	436.4	-	110.9	
	CL-20		0	252.1	-	-	
	LaFeO ₃ /CL-20		20%	247.4	-	-	
	LaFeO ₃ @MnO ₂ /CL-20		20%	245.9	-	-	
	HMX		0	283.0	-	-	
	LaFeO ₃ /HMX		20%	279.9	-	-	
LaFeO ₃ @MnO ₂ /HMX	20%	273.4	-	-			
XY ₂ O ₄	AP	colloidal crystal template	0	413.8	488.2	-	[73]
Nanoporous	CoFe ₂ O ₄ /AP		1%	354.5	950.5	-	
Nanoporous	CoFe ₂ O ₄ /AP		2%	356.0	1120.8	-	
Nanoporous	CoFe ₂ O ₄ /AP		3%	341.0	997.2	-	
Nanoporous	CoFe ₂ O ₄ /AP		4%	328.7	1109.6	-	
Nanoporous	CoFe ₂ O ₄ /AP		5%	329.3	1114.5	74.0	
Nanosphere	CoFe ₂ O ₄ /AP		5%	348.2	-	94.6	
Nanoporous	CoFe ₂ O ₄ /AP		6%	322.4	971.1	-	
Nanoporous	CoFe ₂ O ₄ /AP	7%	327.5	1113.2	-		
XY ₂ O ₄	AP	solvothermal	0	404.3	-	162.3	[79]
	NiFe ₂ O ₄ /AP		10%	322.3	-	-	
	ZnFe ₂ O ₄ /AP		10%	373.4	-	-	
	CoFe ₂ O ₄ /AP		10%	295.3	-	124.9	
Ce doped NiFe ₂ O ₄		sol-gel combustion synthesis	0	432.7	857.0	-	[82]
NiFe ₂ O ₄	NiFe ₂ O ₄ /AP		5%	413.2	1144.0	-	
NiFe ₂ Ce _{0.03} O ₄	NiFe ₂ Ce _{0.03} O ₄ /AP		5%	407.9	1147.0	-	
NiFe ₂ Ce _{0.06} O ₄	NiFe ₂ Ce _{0.06} O ₄ /AP		5%	406.8	1190.0	-	
NiFe ₂ Ce _{0.09} O ₄	NiFe ₂ Ce _{0.09} O ₄ /AP		5%	374.9	1259.0	-	

4. The Preparation of Carbon Composites and Their Application on the EMs

Nanoscale transition MOs used as combustion rate catalysts are proved to be able to effectively promote thermal decomposition of EMs and improve the combustion performance of EMs. Many transition metal oxides, such as CuO, NiO, MnO₂, TiO₂, and Fe₂O₃, have been used as burn rate catalysts for solid propellants. Among them, α -Fe₂O₃ is widely used due to its abundant, low cost, and nontoxic properties. However, the large surface area of this nanoscale catalyst always tends to agglomerate, which was one of the reasons for the reduced catalytic activity. In recent years, carbon materials such as graphene and its derivatives, carbon nanotubes, graphitic carbon nitride, etc., have been used as catalyst support and EMs due to its large specific surface area, excellent mechanical properties, good electrical and thermal conductivity.

4.1. Hematite/Graphene Composites

Since Novoselov obtained single layer graphene sheets by mechanical exfoliation in 2004 [83], graphene has developed rapidly in the fields of basic science and energy engineering. As a single atom thick graphite sheet with a two-dimensional honeycomb structure, it has a large theoretical specific surface area (2630 m² g⁻¹), high electrical conductivity, thermal conductivity and excellent mechanical properties [84]. These years, graphene has shown considerable potential in applications such as biomolecule detection, cell/tissue imaging, energy storage, catalysis, and batteries [82,85–89].

Graphene can affect the size and morphology of nanocrystalline materials and can make nanocrystals evenly distributed on the surface of graphene. It is worth noting that the synergistic effect between graphene and nanoparticles will always bring significantly enhanced performance. These advantages make the preparation and application of nanoparticle/graphene composites become a research hotspot [90–94]. In addition, graphene is also an excellent additive material for the construction of insensitive energetic components, which can be used to improve the safety performance of energetic components [95,96].

Qin et al. [97] used graphene oxide (GO) and ferric nitrate as raw materials to prepare Fe₂O₃/graphene composites by hydrothermal method. In brief, A certain amount of GO was added to deionized water, stirring for 1 h, and then ultrasonicated for 0.5 h to form a good GO suspension. After that, Fe(NO₃)₃·9H₂O was put into a 250 mL three necked flask; then, the GO solution was added, and some aqueous ammonia solution was slowly added dropwise at room temperature until pH = 10–11. After stirring the solution for 2 h, 1 mL of hydrazine hydrate (98%) was added and evenly stirred. Then, the mixture was poured into a 20 mL hydrothermal reactor, reacted at 180 °C for 12 h, cooled to room temperature naturally after the reaction, finally the resulting colloidal product was washed and dried by centrifugation for several times.

Fe₂O₃/G/HMX was tested by DSC at different heating rates, and the effect of heating rate on the thermal decomposition characteristics of HMX and its apparent activation energy was studied.

Our group [98] synthesized two kinds of hematites with different morphologies (rod-like rFe₂O₃ and granular pFe₂O₃) by hydrothermal method. Then, the two composites (rFe₂O₃/G and pFe₂O₃/G) with three dimensional network structure were prepared by interfacial self-assembly method. The catalytic activity of the prepared Fe₂O₃ and Fe₂O₃/G for the thermal decomposition of CL-20 was investigated by DSC.

Figure 16a shows that pure CL-20 has exothermic behavior with peak temperature $T_p = 525.28$ K. Under the catalysis of rFe₂O₃/G, pFe₂O₃/G, rFe₂O₃ and pFe₂O₃, the thermal decomposition peak temperature of CL-20 were reduced by 8.34, 7.69, 6.28 and 5.84 K, respectively. The corresponding TG curves show that the mass loss rate reaches the maximum value at 515.04, 515.75, 516.87 and 517.82 K, which are all lower than pure CL-20 ($T_p = 522.88$ K; Figure 16b).

In addition, the catalytic effect rFe₂O₃/G towards HMX and RDX was also investigated. Figure 17 show that the exothermic decomposition temperatures of pure HMX and RDX at a heating rate of 10 K·min⁻¹ are 556.31 K and 515.65 K, respectively. After mixing with the

prepared catalysts, the decomposition process of HMX and RDX changed significantly. The distinct endothermic melting peak of pure HMX completely disappears after the addition of $r\text{Fe}_2\text{O}_3/\text{G}$ or $r\text{Fe}_2\text{O}_3$. The initial decomposition temperature of $r\text{Fe}_2\text{O}_3/\text{G}/\text{HMX}$ was lower than that of $r\text{Fe}_2\text{O}_3/\text{HMX}$, and the exothermic decomposition peak temperature decreased from 556.31 K to 551.72 K and 553.18 K, respectively. In Figure 17b, although the position of the endothermic temperature of RDX did not change, the exothermic peak changed significantly with the addition of $r\text{Fe}_2\text{O}_3$ or $r\text{Fe}_2\text{O}_3/\text{G}$. A sharp peak appeared in the DSC curve of $r\text{Fe}_2\text{O}_3/\text{RDX}$, and the peak temperature was 507.23 K. Therefore, $\text{Fe}_2\text{O}_3/\text{G}$ particles have stronger catalytic activity for the thermal decomposition of CL-20, HMX and RDX, comparing with the MOs alone. The reason lies in the synergistic effect between Fe_2O_3 and graphene and the high specific surface area of the $\text{Fe}_2\text{O}_3/\text{G}$ composite.

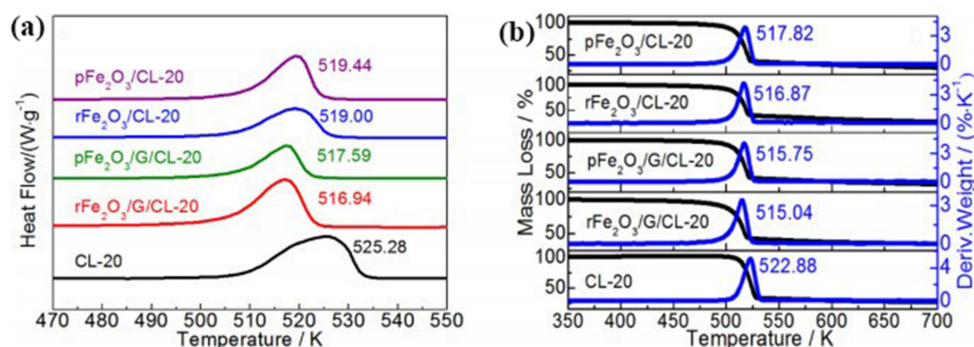


Figure 16. (a) DSC and (b) TG-DTG curves of CL-20 mixed with different catalysts. (a,b) Reproduced with the permission of ref. [98]. Copyright 2020, Acta Physico-Chimica Sinica.

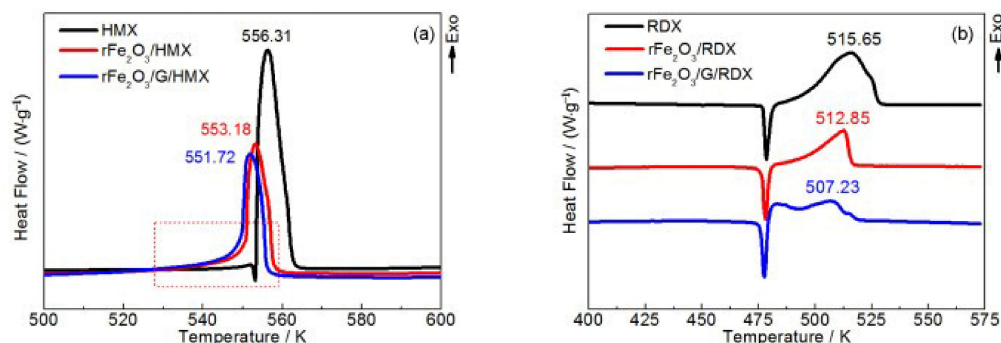


Figure 17. DSC curves of (a) $r\text{Fe}_2\text{O}_3/\text{G}$ and (b) $r\text{Fe}_2\text{O}_3$ mixed with HMX and RDX. (a,b) Reproduced with the permission of ref. [98]. Copyright 2020, Acta Physico-Chimica Sinica.

Therefore, GO could be a good support material to decrease the aggregation degree of single MOs. Pei et al. [99] prepared Fe_2O_3 nano-particles through hydro-thermal method using $\text{FeCl}_3 \cdot 6\text{H}_2\text{O}$ and sodium acetate as raw materials. Then, $\text{Fe}_2\text{O}_3/\text{GO}$ nanocomposites were synthesized by vacuum-freeze-drying. The procedure and the morphology of the Fe_2O_3 and $\text{Fe}_2\text{O}_3/\text{GO}$ was shown in Figure 18. The shape of pure Fe_2O_3 nanoparticles is cubic (Figure 18b) and the average size of the prepared nanoparticles was 36.42 ± 6.47 nm. The Fe_2O_3 nanoparticles were well combined and wrapped by GO flakes (Figure 18d,e).

The catalytic performance of the prepared $\text{Fe}_2\text{O}_3/\text{GO}$ nanocomposites for thermal decomposition of AP was investigated by DSC technique. Figure 19 show the DSC curves of pure AP and AP with 3 wt% ratio of different $\text{Fe}_2\text{O}_3/\text{GO}$ nanocomposites. The admixture catalyst could reduce the onset temperature of the HTD step and decrease the HTD temperature of AP by 77 °C, and the amount of heat released with the catalyst is twice that of pure AP. The reason for this good catalytic activity is because GO provides an ideal supporting substrate for the uniform distribution of Fe_2O_3 nanoparticles; thus, Fe_2O_3 can provide positive holes to accelerate the decomposition process.

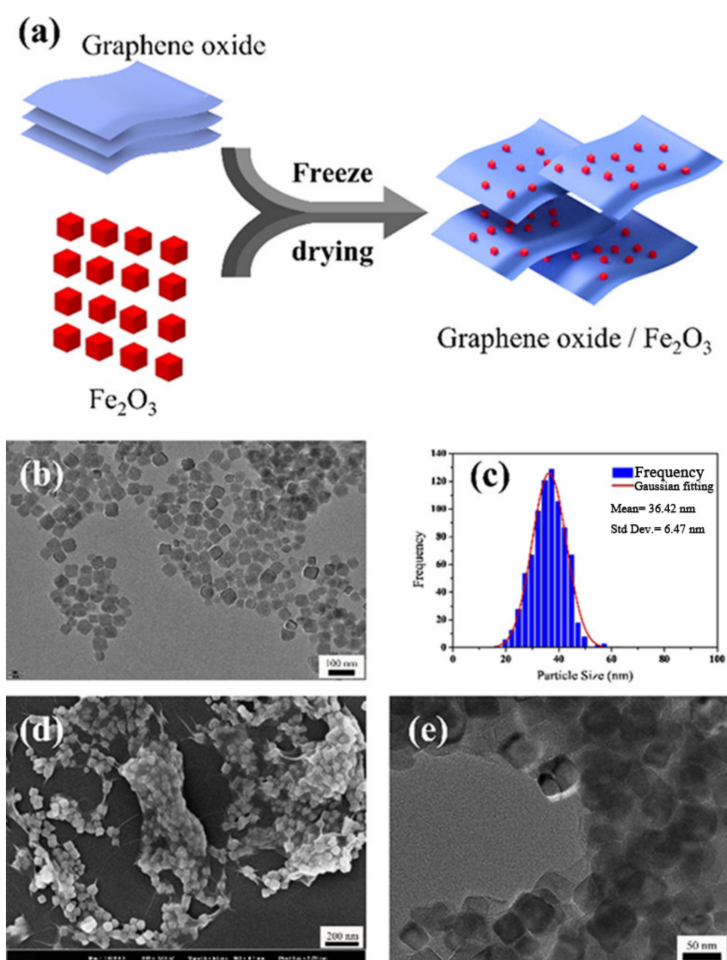


Figure 18. (a) Schematic diagram of the preparation and structure of the GO /Fe₂O₃ hybrid. (b) HRTEM image of the Fe₂O₃nanoparticles, (c) size distribution of Fe₂O₃ nanoparticles. (d) SEM image of sample 1, (e) HRTEM image of sample 1. (a–c) Reproduced with the permission of ref. [99]. Copyright 2021, Langmuir.

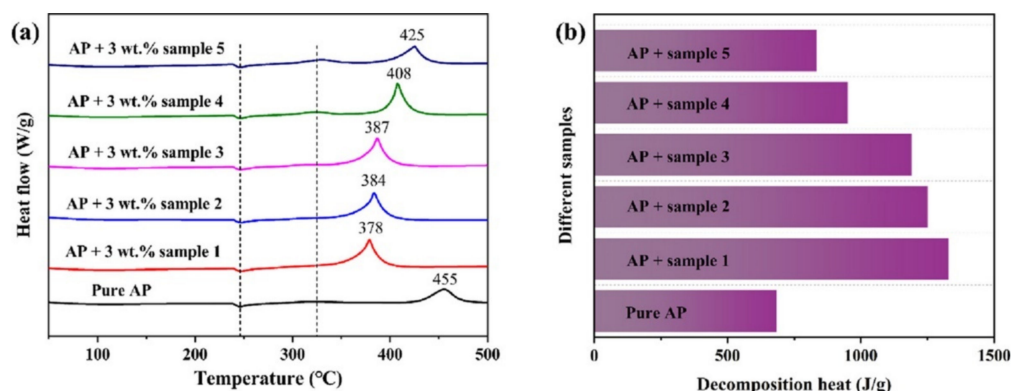


Figure 19. (a) DSC curves of AP thermal decomposition with and without the GO/Fe₂O₃ nanocomposite; (b) heat release during the decomposition of AP with and without catalysts. (a,b) Reproduced with the permission of ref. [99]. Copyright 2021, Langmuir. Sample 1 GO:Fe₂O₃ = 1:10, Sample 2 GO:Fe₂O₃ = 3:20, Sample 3 GO:Fe₂O₃ = 3:10, Sample 4 GO:Fe₂O₃ = 1:1, Sample 5 GO:Fe₂O₃ = 3:1.

Fertassi et al. [100] used ferric chloride hexahydrate (FeCl₃·6H₂O) as the precursor to prepare α -Fe₂O₃ nanoparticles by hydrothermal method. GO was synthesized using a modified Hummers method, and rGO were successfully obtained by thermal reduction of

GO. α -Fe₂O₃/rGO nanocomposites were prepared using ex situ synthesis in the presence of α -Fe₂O₃ nanoparticles and GO solution. The catalytic activity towards the thermal decomposition of AP was investigated. DTA results show that the obtained nanomaterials help to improve the thermal decomposition of AP; specifically, the HTD of AP is reduced from 432 to 380 °C. In the presence of these nanomaterials, the activation energy was also significantly reduced from 129 to 80.33 kJ·mol⁻¹.

The solvent used in the solvothermal method has a great influence on the structure and properties of the synthesized materials. Zhang et al. [101] prepared Fe₂O₃/rGO composites by a hydro-thermal method using six different solvents (distilled water, ethanol, N-methylpyrrolidone, ethyl acetate, n-butanol, and N,N-dimethylformamide). The specific synthesis route and catalytic mechanism of thermal decomposition of AP are shown in Figure 20. Fe(NO₃)₃ and GO suspension were sealed in the Teflon reactor for 24 h at 180 °C. After washing and drying, the Fe₂O₃/rGO composite was obtained. The SEM results showed that the Fe₂O₃ nanoparticles were successfully anchored on the graphene surface (Figure 21a–e). However, the morphology of the composites and the dispersion of Fe₂O₃ nanoparticles were found to be significantly different with different solvents. Compared with the Fe₂O₃/rGO composites prepared in NBA, H₂O, NMP, EA and EG solvents, the composites obtained in DMF solvent exhibited a thinner structure. Equally importantly, the distribution of Fe₂O₃ nanoparticles immobilized on graphene was also high using DMF as the reaction solvent, confirming that graphene can effectively prevent the aggregation of Fe₂O₃ nanoparticles. GO and rGO can significantly contribute to the better dispersion properties of nano particles [102,103].

In the presence of Fe₂O₃/rGO (DMF) composites, the HTD and apparent activation energy of AP decreased by 119.6 °C and 173.3 kJ·mol⁻¹, respectively.

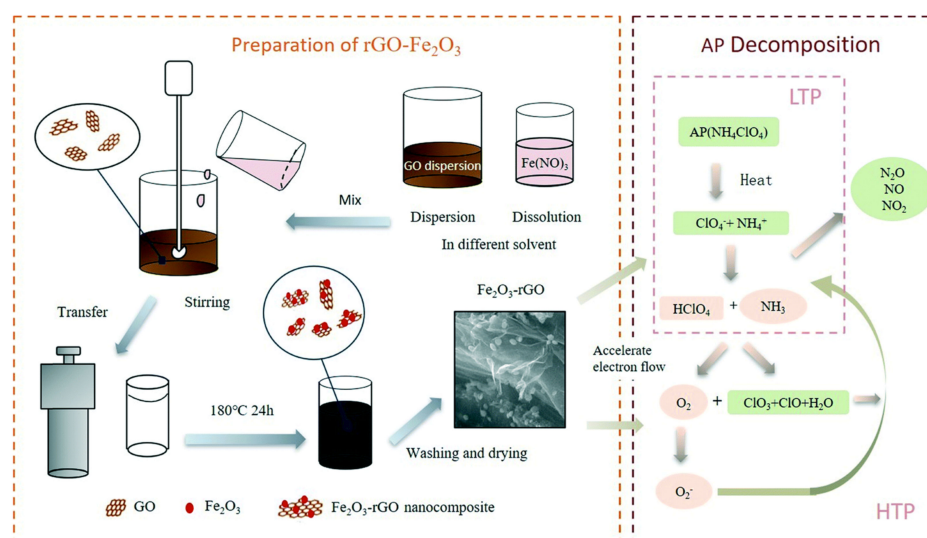


Figure 20. Illustration of Fe₂O₃/rGO fabrication and its catalytic mechanism for the thermal decomposition of AP. Reproduced with the permission of ref. [101]. Copyright 2018, Crystengcomm.

Atomic Layer Deposition (ALD) is a thin film coating technique that enables the production of nanometer films or nanoparticles in a highly controlled manner. Yan et al. [104] prepared rGO@Fe₂O₃ with finely dispersed Fe₂O₃ nanoparticles using the ALD route. Fe₂O₃ nanoparticles with uniform particle size are uniformly anchored to rGO nanosheets through surface chemical interactions, thus effectively suppressing the aggregation of Fe₂O₃ nanoparticles, and graphene nanosheets have high specific surface area and excellent electrical conductivity, which can increase the accessibility number of active sites and enhance electron transfer during catalysis. The morphologies of the prepared rGO@Fe₂O₃ was show in Figure 22a,b. DSC results in Figure 22c indicate that the presence of 5 wt% rGO@Fe₂O₃ composite makes the two decomposition stages of pristine AP almost merge into a single

exothermic peak between the LTD and HTD stages. The rGO@Fe₂O₃ with 212 wt% of Fe₂O₃ on the rGO bases exhibits a significantly lower decomposition temperature compared with those of rGO and rGO@Fe₂O₃ composites.

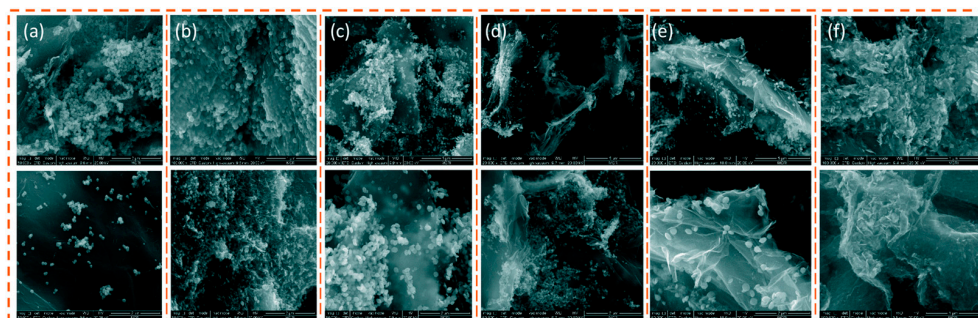


Figure 21. SEM and TEM images of Fe₂O₃/rGO composites fabricated in different solvents: (a) NBA, (b) H₂O, (c) EA, (d) NMP, (e) DMF, and (f) EG. (a–f) Reproduced with the permission of ref. [101]. Copyright 2018, Crystengcomm.

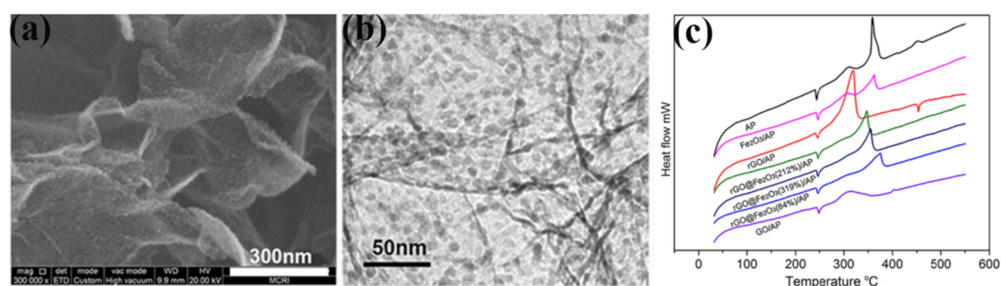


Figure 22. SEM images of (a) rGO@(84wt%)Fe₂O₃, and TEM images of (b) rGO@(84wt%)Fe₂O₃; (c) DSC curves for the thermal decomposition of AP with different additives. (a–c) Reproduced with the permission of ref. [104]. Copyright 2018, Applied Surface Science.

There are some other methods for preparing the Fe₂O₃/rGO composite. Elbasuney et al. [105] effectively prepared Fe₂O₃/rGO nanocomposites using a solution co-precipitation method in deionized water. After adding a hydrazine reducing agent, washing, centrifuging and drying, the composite nano particles were developed via calcinations at 400 °C. The TEM images of Fe₂O₃/rGO show that the hybrid nanocomposites consist of two-dimensional rGO sheets and were decorated with Fe₂O₃ nanocrystal. The catalytic performance of the Fe₂O₃/rGO nanocomposite towards the thermal behavior of AP was evaluated using DSC and TGA. The initial endothermic decomposition of AP is reduced by 16% and the total heat release was improved by 83%. The combination of rGO and Fe₂O₃ provides a high interfacial surface area, which can ensure the absorption of gaseous products on the catalyst surface with a surge in the total heat release.

4.2. Ferrite/Graphene Composites

Ferrite-based burn rate modifiers contain two metal elements, which may have catalytic effects on both elements. Carbon materials have been widely used as additives in solid propellants. Different methods are used to load ferrite nanoparticles on the surface of carbon materials, so that the catalyst has the advantage of both bimetallic elements and carbon materials. This type of composite material has the effect of reducing the migration ability of nanoparticles, which is of great significance to the long-term storage stability of propellants.

Xu et al. [106] prepared bismuth ferrite/graphene (BiFeO₃/rGO) nanocomposites by a hydrothermal method using graphene oxide as a carrier. The effect of different addition amounts of BiFeO₃/rGO nanocomposites on the thermal decomposition properties of AP was studied by differential thermal analysis. In order to study the effect of catalyst content

on the thermal decomposition performance of AP, 1 wt%, 2 wt%, 3 wt%, 4 wt% and 5 wt% of BiFeO₃/GO nanocomposites were added to AP, respectively. The results show that the BiFeO₃/rGO nanocomposite has a good ability to catalyze the thermal decomposition of AP. When the mass fraction of BiFeO₃/rGO nanocomposite is 4 wt%, the thermal decomposition catalytic performance is the best (reduce the HTD by 167 °C). The catalytic activity of BiFeO₃/rGO nanocomposite was believed to accelerate the thermal decomposition reaction of AP. The high catalytic effect benefits from its nano-sized morphology and large specific surface area, which can provide more active reaction sites, and can fully react with AP.

The catalytic effect of bismuth ferrite is different from iron oxide, and obviously also different from the mixture of iron oxide and bismuth oxide. Guo et al. [107] used the hydrothermal method to prepare BiFeO₃/GO, K and Ce doped BiFeO₃/GO. The effect of doping on the particle size of bismuth ferrite was further confirmed by TEM (Figure 23a,b). The nanoparticles in K/BiFeO₃/GO are 10–100 nanometers, and the Ce/BiFeO₃/GO sample presents a large number of tiny particles with a size less than 20 nm. To study the catalytic thermal decomposition ability of the catalyst to the high energy explosive HMX, the catalyst and HMX were ground and mixed at a mass ratio of 1:4. The results are shown in Figure 23c,d, BiFeO₃/GO doped with cerium ions showed a good catalytic effect on the thermal decomposition of HMX, and the onset temperature of thermal decomposition was advanced from 281 °C to 209 °C. Since Ce/BiFeO₃/GO directly decomposes HMX in the solid phase, the initial decomposition temperature is greatly increased, indicating that it has a higher catalytic thermal decomposition activity than K/BiFeO₃/GO.

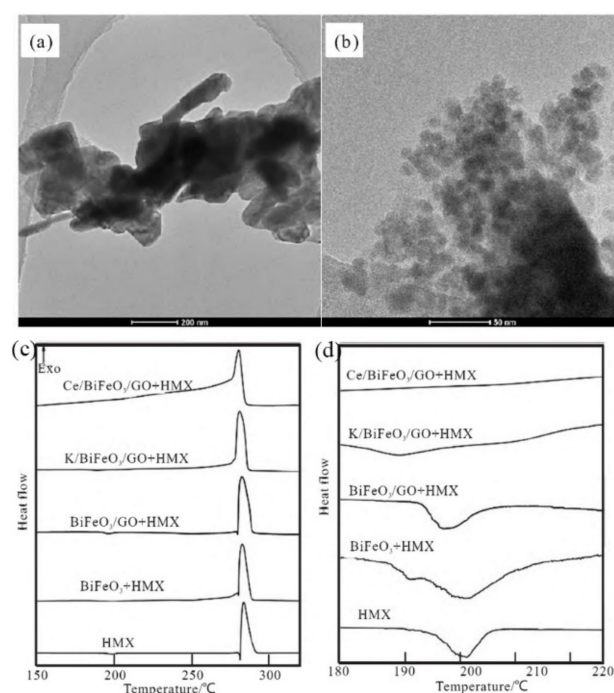


Figure 23. TEM images of (a,b) K doped BiFeO₃/GO and Ce doped BiFeO₃/GO; DSC curves of (c,d) HMX and the mixtures of HMX with four different BiFeO₃ composites. (a–d) Reproduced with the permission of ref. [107]. Copyright 2022, Journal of Solid Rocket Technology.

The improved catalytic activity due to the synergistic effect of nanoparticles and rGO, which may broaden new applications in modifying the combustion behavior of AP-based composite propellants. Chen et al. [108] successfully prepared CoFe₂O₄/rGO hybrids by a facile one-pot solvothermal method, and their catalytic behavior for AP decomposition was investigated by varying their content in the range of 1–5% by differential thermal analysis. It was confirmed by TEM Figure 24a,b that rGO can effectively prevent the aggregation of CoFe₂O₄ nanoparticles. The synthesized CoFe₂O₄/rGO hybrid exhibited high catalytic activity for the thermal decomposition of AP, as shown in Figure 24c,d. The

HTD temperature gradually decreased with the increase in the catalyst. After adding a 3% $\text{CoFe}_2\text{O}_4/\text{rGO}$ hybrid, the HTD temperature of AP decreased by $104.7\text{ }^\circ\text{C}$, which was lower than that of bare CoFe_2O_4 with the same proportion. Thus, rGO can enhance the catalytic activity of CoFe_2O_4 and facilitate the thermal decomposition process. The improved catalytic activity may broaden new applications in modifying the combustion behavior of AP-based composite propellants.

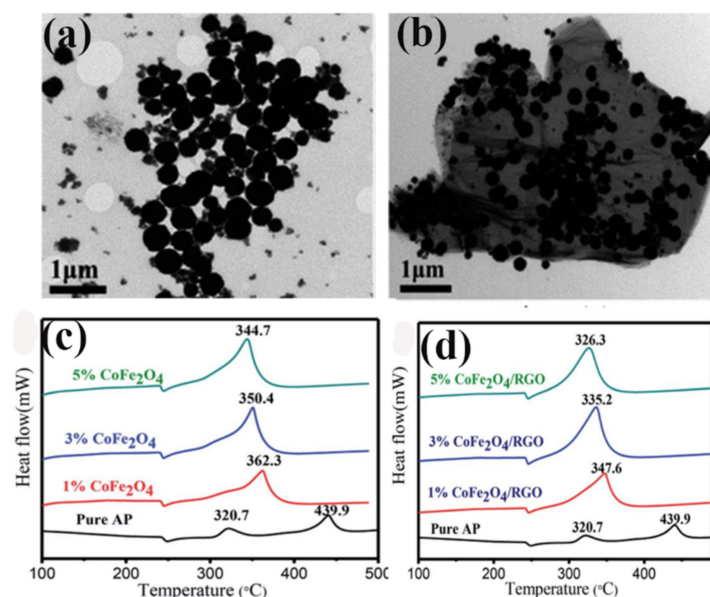


Figure 24. TEM images of (a) the as-synthesized CoFe_2O_4 ; (b) $\text{CoFe}_2\text{O}_4/\text{RGO}$ hybrids. (c) DTA curves of pure AP and AP mixed with CoFe_2O_4 (1%, 3%, and 5%), (d) pure AP and AP mixed with $\text{CoFe}_2\text{O}_4/\text{RGO}$ hybrids (1%, 3%, and 5%). (a–d) Reproduced with the permission of ref. [108]. Copyright 2016, RSC Advances.

They also successfully synthesized $\text{NiFe}_2\text{O}_4/\text{rGO}$ nanoparticles by the solvothermal method [109]. The catalytic activity of the synthesized $\text{NiFe}_2\text{O}_4/\text{rGO}$ nanoparticles on AP was characterized by DSC. The DSC curves show that with the addition of $\text{NiFe}_2\text{O}_4/\text{rGO}$ nanoparticles, the LTD and the HTD merge into a single exothermic process, but the phase transition temperature position of AP still exists as AP. The HTD temperature decreases gradually with the increase content of the catalyst. Compared with pure AP, the HTD temperature of AP decreased by $103.8\text{ }^\circ\text{C}$ when adding 5% $\text{NiFe}_2\text{O}_4/\text{rGO}$.

Wang et al. [110] also prepared $\text{ZnFe}_2\text{O}_4/\text{rGO}$ nanohybrids by a facile one-pot hydrothermal method. The TEM images confirmed that the ZnFe_2O_4 NPs with a size of about 10 nm were anchored uniformly on the rGO sheet. DSC results indicated that $\text{ZnFe}_2\text{O}_4/\text{rGO}$ nanohybrids exhibited enhanced catalytic activity for the thermal decomposition of AP compared with ZnFe_2O_4 NPs. The composites can reduce the secondary decomposition temperature of AP by $42.7\text{ }^\circ\text{C}$, $55.0\text{ }^\circ\text{C}$ and $68.1\text{ }^\circ\text{C}$ with the increase in the proportion (1%, 3%, 5%), respectively. Furthermore, the composite with the proportion of $\text{ZnFe}_2\text{O}_4/\text{rGO}$ reduces the apparent activation energy of AP from 160.2 kJ mol^{-1} to 103.8 kJ mol^{-1} . rGO is supposed to accelerate the electron flow, which can further accelerate the heterogeneous decomposition reaction rate of gas-phase molecules on the surface of NPs.

4.3. Carbon Nanotubes

Carbon nanotubes (CNTs) have nano-scale lumen structure, large specific surface area, surface energy and surface binding energy, and graphite like multi-layer tube wall structure, which can adsorb and fill particles. Moreover, with good chemical stability, good electrical conductivity and high mechanical strength, loading nanocatalysts on CNTs can improve the dispersion problem of nanoparticles and promote the transfer of electrons during the

reaction, increase the catalytic effect, which makes it have a good application prospect in the catalyst carrier [111,112]. CNTs, as the adsorptive carrier for Fe_2O_3 , can maximize the specific surface area of the prepared nanoscale Fe_2O_3 catalysts, thereby improving its catalytic efficiency.

Wang et al. [113] used the liquid-phase precipitation to prepare $\text{Fe}_2\text{O}_3/\text{CNTs}$ composites. Additionally, the $\text{Fe}_2\text{O}_3/\text{CNTs}$ composite nanocatalyst was found to be able to significantly reduce the decomposition temperature of AP and improve the burning rate of AP unit propellant. The catalytic activity of $\text{Fe}_2\text{O}_3/\text{CNTs}$ composite for AP is better than that of nano- Fe_2O_3 and the simple mixture of nano- Fe_2O_3 and CNTs.

Jiang et al. [114] used purified CNTs as a carrier to prepare $\text{Fe}_2\text{O}_3/\text{CNTs}$ composite particles by a sol-gel method. Figure 25a,b shows the SEM image of $\text{Fe}_2\text{O}_3/\text{CNTs}$ and the DSC curves of the composite with a different ratio. The characterization indicated that the Fe_2O_3 nano-particles stuck on the surface of CNTs. $\text{Fe}_2\text{O}_3/\text{CNTs}$ composite particles with a molar ratio of 1:7 can apparently decrease the thermal decomposition peak temperature of AP to 345.8 °C, reducing the apparent activation energy of AP from 178 $\text{kJ}\cdot\text{mol}^{-1}$ to 118 $\text{kJ}\cdot\text{mol}^{-1}$.

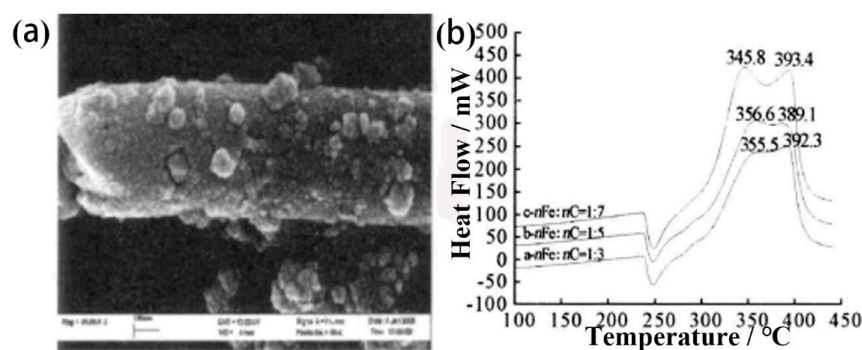


Figure 25. (a) SEM image of $\text{Fe}_2\text{O}_3/\text{CNTs}$ composite particles; (b) DSC curves of AP with different ratio of $n\text{Fe}_2\text{O}_3:n\text{CNTs}$. (a,b) Reproduced with the permission of ref. [114]. Copyright 2008, Journal of Solid Rocket Technology. Cui et al. [115] used ferric nitrate as raw material, citric acid as chelating agent, adjusted the pH value with ammonia water to obtain a uniformly dispersed CNTs sol, and prepared nano- $\text{Fe}_2\text{O}_3/\text{CNTs}$ catalyst by the sol-gel method. The nanoscaled Fe_2O_3 particles are found to be uniformly coated on the surface of CNTs. The effect of $\text{Fe}_2\text{O}_3/\text{CNTs}$ on the thermal decomposition performance of RDX was investigated by DSC. The 5 wt% added $\text{Fe}_2\text{O}_3/\text{CNTs}$ composite particles were capable of reducing the decomposition peak temperature and the activation energy of RDX by 14.1 °C and 42.03 $\text{kJ}\cdot\text{mol}^{-1}$, respectively.

4.4. Graphitic Carbon Nitride

Graphitic carbon nitride ($g\text{-C}_3\text{N}_4$) has attracted much attention as a new generation of green non-metallic two-dimensional catalysts. In the typical structure of $g\text{-C}_3\text{N}_4$, C and N atoms form a highly delocalized large π -conjugated system by sp^2 hybridization, becoming the lowest energy but most stable carbon nitride allotrope [116]. There are some reports related to the good photoelectrochemical catalytic performance [117–119], which indicates that the $g\text{-C}_3\text{N}_4$ does much contribution to reducing the bandgap, escalating the specific area of the made composite. In the EMs field, it was reported that adding 10% $g\text{-C}_3\text{N}_4$ to AP can advance the pyrolysis peak temperature of AP by 70 °C [120].

Wang et al. [121] prepared $\text{Fe}_2\text{O}_3/g\text{-C}_3\text{N}_4$ composite using $\text{FeCl}_3\cdot 6\text{H}_2\text{O}$ and melamine as the precursors by sol-gel method. The SEM image indicates that Fe_2O_3 particles are tightly supported by $g\text{-C}_3\text{N}_4$. The catalytic effect of the prepared composite on the thermal decomposition of AP was investigated by DSC. DSC tests showed that the addition of the composite catalysts with 5% mass fractions reduced the HTD and LTD of AP to 348.1 °C and 281.7 °C, respectively.

The properties of ferrite nano particles with $g\text{-C}_3\text{N}_4$ were studied by some researchers. Wan et al. [122] self-assembly combined CoFe_2O_4 with a prepared $g\text{-C}_3\text{N}_4$ using $\text{Fe}(\text{NO}_3)_3 \cdot 9\text{H}_2\text{O}$ and $\text{Co}(\text{NO}_3)_2 \cdot 6\text{H}_2\text{O}$ as precursors in a hydrothermal environment. DSC results show (Figure 26) that $\text{CoFe}_2\text{O}_4/g\text{-C}_3\text{N}_4$ reduces the thermal decomposition peak temperature of HMX and TKX-50 by $7.0\text{ }^\circ\text{C}$ and $41.3\text{ }^\circ\text{C}$, respectively, and the apparent activation energy decreases by $341.1\text{ kJ}\cdot\text{mol}^{-1}$ and $21.0\text{ kJ}\cdot\text{mol}^{-1}$. The as-prepared composite have a better catalytic effect on HMX and HATO(TKX-50). Now some other literatures [123] involved $g\text{-C}_3\text{N}_4$ as a carrier show that this carbon material exhibits good catalytic effect on the thermal decomposition of EMs. Thus, $g\text{-C}_3\text{N}_4$ may be a prospective application as a combustion catalysis.

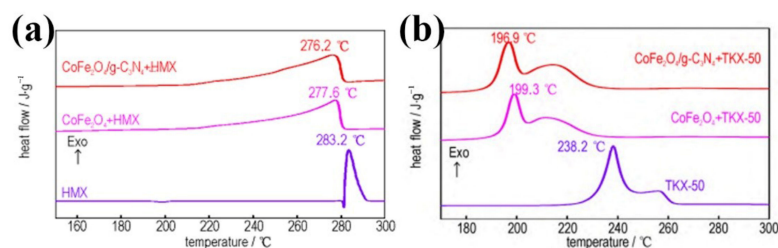


Figure 26. DSC curves of (a) HMX, CoFe_2O_4 +HMX and $\text{CoFe}_2\text{O}_4/g\text{-C}_3\text{N}_4$ +HMX; (b) DSC curves of TKX-50, CoFe_2O_4 +TKX-50 and $\text{CoFe}_2\text{O}_4/g\text{-C}_3\text{N}_4$ +TKX-50. (a,b) Reproduced with the permission of ref. [122]. Copyright 2022, Journal of Energetic Materials.

Table 3 summarizes the related preparation methods and corresponding thermal parameters in recent years. Carbon materials, especially graphene, contribute much to the enhancement of the catalytic effect of EMs due to the synergistic effect of NPs and rGO.

Table 3. Summary of thermal behavior parameters of carbon composites EMs.

Materials	Samples	Preparation Method	Mass Ratios	T_p	ΔH	E	Refs.
GO	$\text{Fe}_2\text{O}_3/\text{GO}/\text{HMX}$	hydrothermal	1%	242.6	-	139.9	[97]
G	CL-20	hydrothermal	0	252.1	179.2	183.4	[98]
	$p\text{Fe}_2\text{O}_3/\text{CL-20}$		20%	246.3	-	172.6	
	$r\text{Fe}_2\text{O}_3/\text{CL-20}$		20%	245.9	161.5	165.6	
	$p\text{Fe}_2\text{O}_3/\text{G}/\text{CL-20}$		20%	244.4	-	159.9	
	$r\text{Fe}_2\text{O}_3/\text{G}/\text{CL-20}$		20%	243.8	148.9	153.0	
	HMX		0	283.2	-	-	
	$r\text{Fe}_2\text{O}_3/\text{HMX}$		20%	280.0	-	-	
	$r\text{Fe}_2\text{O}_3/\text{G}/\text{HMX}$		20%	278.6	-	-	
	RDX		0	242.5	-	-	
	$r\text{Fe}_2\text{O}_3/\text{RDX}$		20%	239.7	-	-	
	$r\text{Fe}_2\text{O}_3/\text{G}/\text{RDX}$		20%	234.1	-	-	
GO	AP	vacuum-freeze-drying	0	455.0	-	-	[99]
Sample 1	10:1 $\text{Fe}_2\text{O}_3/\text{GO}/\text{AP}$		3%	378.0	-	-	
Sample 2	20:3 $\text{Fe}_2\text{O}_3/\text{GO}/\text{AP}$		3%	384.0	-	-	
Sample 3	10:3 $\text{Fe}_2\text{O}_3/\text{GO}/\text{AP}$		3%	387.0	-	-	
Sample 4	1:1 $\text{Fe}_2\text{O}_3/\text{GO}/\text{AP}$		3%	408.0	-	-	
Sample 5	3:1 $\text{Fe}_2\text{O}_3/\text{GO}/\text{AP}$		3%	425.0	-	-	
GO	AP	hydrothermal	0	432.0	-	129.0	[100]
	GO/AP		1.84%	400.0	-	100.1	
	$\text{Fe}_2\text{O}_3/\text{AP}$		1.84%	397.0	-	89.3	
	$\text{Fe}_2\text{O}_3/\text{G}/\text{AP}$		1.84%	380.0	-	80.3	
GO	AP	solvothermal	0	440.8	-	290.0	[101]
	GO/AP		5%	372.5	-	216.2	
H_2O	rGO/AP		5%	360.8	-	128.8	
H_2O	$\text{Fe}_2\text{O}_3/\text{AP}$		5%	369.4	-	170.3	
DMF	$\text{Fe}_2\text{O}_3/\text{rGO}/\text{AP}$		5%	321.2	-	119.8	
rGO	AP	atomic layer deposition	0	440 ± 5	-	-	[104]

Table 3. Cont.

Materials	Samples	Preparation Method	Mass Ratios	T_p	ΔH	E	Refs.
rGO	Fe ₂ O ₃ /rGO/AP	direct precipitation	5%	358	-	-	[105]
	AP		0	425.8	-	-	
rGO	Fe ₂ O ₃ /rGO/AP	hydrothermal	1%	413.1	-	-	[106]
	AP		0	462.0	887.0	172.1	
	BiFeO ₃ /AP		-	449.0	-	144.5	
	1% BiFeO ₃ /rGO/AP		-	427.0	-	-	
	2% BiFeO ₃ /rGO/AP		-	396.0	-	-	
	3% BiFeO ₃ /rGO/AP		-	354.0	-	-	
	4% BiFeO ₃ /rGO/AP		-	295.0	2518.0	128.4	
	5% BiFeO ₃ /rGO/AP		-	308.0	-	-	
GO	HMX	hydrothermal	0	283.4	-	-	[107]
	BiFeO ₃ /HMX		20%	282.7	-	-	
	BiFeO ₃ /GO/HMX		20%	282.4	-	-	
	K/BiFeO ₃ /GO/HMX		20%	280.9	-	-	
	Ce/BiFeO ₃ /GO/HMX		20%	280.5	-	-	
rGO	AP	one-pot solvothermal	0	439.9	-	147.6	[108]
	1% CoFe ₂ O ₄ /AP		-	362.3	-	-	
	3% CoFe ₂ O ₄ /AP		-	350.4	-	131.5	
	5% CoFe ₂ O ₄ /AP		-	344.7	-	-	
	1% CoFe ₂ O ₄ /rGO/AP		-	347.6	-	-	
	3% CoFe ₂ O ₄ /rGO/AP		-	335.2	-	117.9	
rGO	AP	solvothermal	0	439.9	-	147.6	[109]
	3% rGO/AP		-	433.7	-	-	
	3% NiFe ₂ O ₄ /AP		-	363.4	-	-	
	1% NiFe ₂ O ₄ /rGO/AP		-	359.2	-	-	
	3% NiFe ₂ O ₄ /rGO/AP		-	347.3	-	128.3	
	5% NiFe ₂ O ₄ /rGO/AP		-	336.1	-	-	
rGO	AP	one-step hydrothermal	0	424.7	-	160.3	[110]
	ZnFe ₂ O ₄ /AP		1%	380.7	-	-	
	ZnFe ₂ O ₄ /AP		3%	365.0	-	-	
	ZnFe ₂ O ₄ /AP		5%	360.8	-	143.7	
	ZnFe ₂ O ₄ /rGO/AP		1%	380	-	-	
	ZnFe ₂ O ₄ /rGO/AP		3%	367.7	-	-	
	ZnFe ₂ O ₄ /rGO/AP		5%	354.6	-	127.6	
CNTs	AP	sol-gel	0	478.1	-	178.0	[114]
	simple mix		2%	390.9	-	134.0	
	Fe ₂ O ₃ /CNTs/AP particle composite		2%	376.0	-	118.0	
CNTs	RDX	sol-gel	0	240.9	-	109.2	[115]
	Fe ₂ O ₃ /CNTs/RDX		5%	226.8	-	67.17	
g-C ₃ N ₄	AP	direct copolymerization	0	454.4	-	216.0	[120]
g-C ₃ N ₄	g-C ₃ N ₄ /AP	In situ	10%	384.4	-	119.8	[121]
	AP		0	437.4	-	-	
g-C ₃ N ₄	1% Fe ₂ O ₃ /C ₃ N ₄ /AP	solvothermal	2%	376.2	-	-	[122]
	2% Fe ₂ O ₃ /C ₃ N ₄ /AP		2%	368.5	-	-	
	3% Fe ₂ O ₃ /C ₃ N ₄ /AP		2%	358.9	-	-	
	5% Fe ₂ O ₃ /C ₃ N ₄ /AP		2%	348.1	-	-	
	HMX		0	283.2	-	502.2	
	CoFe ₂ O ₄ /HMX		20%	277.6	-	225.6	
	CoFe ₂ O ₄ /g-C ₃ N ₄ /HMX		-	276.2	-	161.1	
TKX-50	-	238.2	-	172.1			
CoFe ₂ O ₄ /TKX-50	-	199.3	-	159.8			
CoFe ₂ O ₄ /g-C ₃ N ₄ /TKX-50	-	196.9	-	151.1			

Note: T (°C); ΔH (J·g⁻¹); E (kJ·mol⁻¹).

5. The Nano-Thermite and Their Application

For the traditional micro-thermite system, there are many unfavorable factors: large component size, uneven mixing, high ignition temperature ($>900\text{ }^{\circ}\text{C}$), slow burning rate and incomplete burning, while when the particle components are nanosized, the contact area and the degree of bonding between the components can be greatly increased.

Nano-thermite is defined as a metastable intermixed composites (MICs) of nano-aluminum powder and nano-metal oxide [124,125]. After compounding in a certain proportion, under the condition of heating or mechanical impact, the violent redox reaction happened, and a large amount of heat released. The early thermite was mainly prepared from Al powder and different MOs in a certain ratio, and it was ignited to generate Al_2O_3 and metals to release a lot of heat. With the development of technology, in addition to aluminum powder, some other active metals such as magnesium, lithium, nickel and boron can also be mixed with metal oxides, and a similar aluminothermic reaction occurs.

At present, nano-thermite is widely used in the fields of pyrotechnics, explosives and rocket propellants. Usually nano-thermite used in solid propellants can improve its specific impulse and combustion efficiency and enhance mechanical properties. Studies have shown that in composite propellants, when nano-aluminum powder replaces ordinary aluminum powder, the propellant burning rate can be increased by 2 to 5 times. Compared with ordinary ignition powder, the biggest advantage of nano-thermite modified ignition powder is that it can generate a lot of heat during the reaction and can reduce the electrostatic discharge sensitivity of nano-thermite ignition powder. In addition, the compounded composite materials can change the agglomeration of the individual nano-aluminum powder; at the same time, the compounded nano-thermite can ensure the active content and increase the contact area so as to improve the combustion performance of solid propellants [126–131].

5.1. Influence of Fuel Additives on Nano-Thermite

The traditional thermite always uses aluminum powder as fuel; however, the exothermic performance sometimes cannot meet the current industrial production. Adding some fuel additives can improve the heat release of the Al/ Fe_2O_3 thermite.

Nie et al. [132] prepared bimetallic thermite powder (Al/ Fe_2O_3 /Ni) by an ultrasonic physical mixing method. They carried out experiments about the aged samples at two relative humidity (RH) levels in air under an isothermal environment ($\sim 60\text{ }^{\circ}\text{C}$). The measured total energy output of the aged and fresh samples with different nickel contents indicated that the energy output in powders with a moderate humidity level of 20% was comparable across the nickel range within 20%. Under extreme humidity conditions of 75%, the energy output of the Ni-free Al/ Fe_2O_3 nanothermite powder was significantly reduced by 33%. Thus, Ni can reduce the sensitivity of nano-thermite powder to humidity at higher temperature, which can prolong the shelf life of the thermite powder.

Shen et al. [133] successfully prepared Al/B/ Fe_2O_3 nano-thermite by the sol-gel method using ultrasonic under mild and non-toxic conditions. The characterizations indicated that nano-aluminum and micro-boron were uniformly dispersed in the pores of the iron oxide gel. DSC tests show that the temperature of the exothermic reaction heat of Al/B/ Fe_2O_3 nanothermites shifts to a lower temperature and the heat release obtained by the sol-gel approach is more than that of the simply physical mixture. Boron was also found to have the highest volumetric heat of combustion, so it is a good choice as a fuel additive in thermite.

Recently, our group [134] prepared bismuth cation-doped hematite (Bi- Fe_2O_3) with different Bi content by a one-step hydrothermal method and used it as a thermal decomposition catalyst for EMs and oxidants in Al-based thermite (Al/Bi- Fe_2O_3). SEM images (Figure 27a–e) show a three-dimensional flower-structure when doping with different molar ratio of Bi/Fe is 0.2 or 0.3. The aluminothermic reaction was evaluated by DSC in the temperature range of $40\text{--}900\text{ }^{\circ}\text{C}$, as shown in Figure 27f. The thermite reaction of Al/Bi- Fe_2O_3 is exothermic with the peak temperatures appearing at $583\text{--}739\text{ }^{\circ}\text{C}$. With the

increase in Bi, the temperature of the first exothermic peak of Al/Bi_x-Fe₂O₃ hybrids is delayed by 6–15 °C, but their second exothermic peak temperature decreases by 58–101 °C. However, the energy release is lower than Al/Fe₂O₃ and decreases with the increasing doping content of Bi. Al/Bi-Fe₂O₃ showed a shorter ignition delay time than Al/Fe₂O₃.

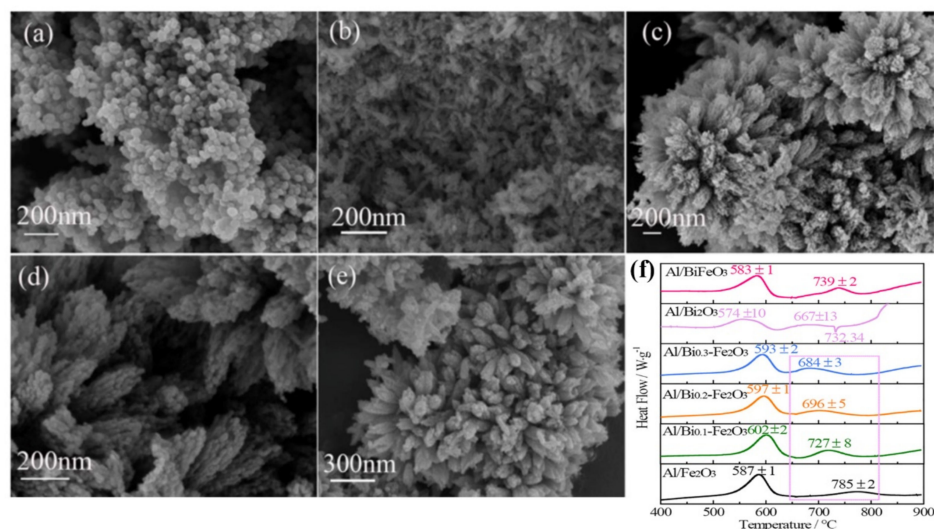


Figure 27. SEM images of (a) Fe₂O₃ and (b) Bi_{0.1}-Fe₂O₃; (c,d) low and high magnification images of Bi_{0.2}-Fe₂O₃; (e) SEM image of Bi_{0.3}-Fe₂O₃; (f) DSC curve of six thermites obtained with a heating rate of 10 °C·min⁻¹ under N₂ flow. (a–f) Reproduced with the permission of ref. [134]. Copyright 2021, Chemical Engineering Journal.

The combustion process of the Al/Bi-Fe₂O₃ thermites with different Bi doping content was tested by CO₂ continuous laser and recorded by a high-speed camera (Figure 28). With the increase in the Bi doping content, the ignition delay time decreases and Bi_{0.3}-Fe₂O₃ can minimize the delay time of Fe₂O₃ most.

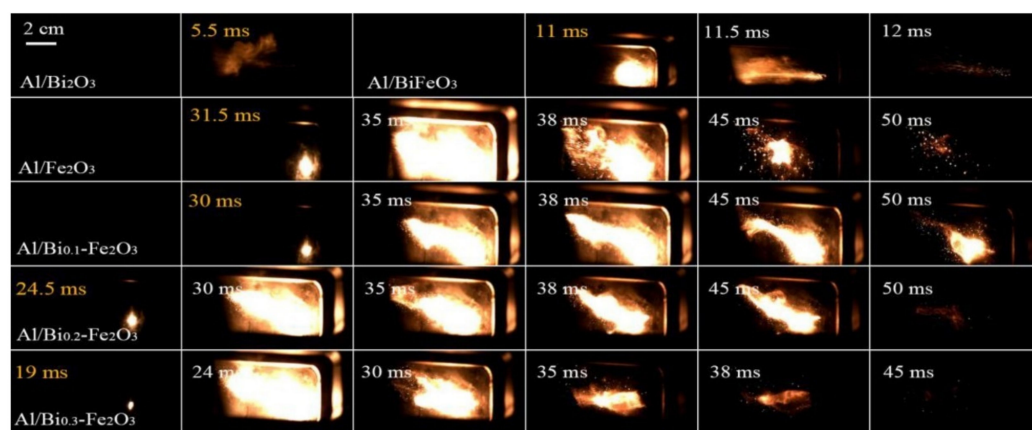


Figure 28. Sequential images of Al/Fe₂O₃, Al/Bi doped Fe₂O₃, Al/Bi₂O₃ and Al/BiFeO₃ combustion process in ambient condition. Reproduced with the permission of ref. [134]. Copyright 2021, Chemical Engineering Journal.

5.2. Influence of Oxidant and Structure on Nano-Thermite

The combustion of nano-thermite is a complex multiphase reaction process, including heat conduction, convection, feedback and radiation. Usually, uniform distribution and closeness means close interfacial contact and short mass transfer and heat diffusion distances between components, which will contribute to promoting the reaction kinetics and improving the combustion performance of the thermite. Thus, various interface

control techniques, such as atomic layer deposition [135], self-assembly [136], sol-gel synthesis [137], electrophoretic deposition [138], in situ growth [139], and arrested reactive milling [140], were used.

The type of oxidant in the thermite is one of the important factors in the exothermic, ignition and combustion properties of composites [141,142]. In the past few decades, many studies of thermite have focused on the preparation and performance improvement of Al/CuO, Al/Fe₂O₃, Al/Bi₂O₃, Al/NiO, Al/WO₃ MICs, in which the oxidants mainly focus on metal oxidation objects [141–146]. Wu et al. [145] studied the thermal behavior of four commonly used thermite systems in different atmospheres: Al/CuO, Al/Fe₂O₃, Al/Fe₃O₄, and Al/Co₃O₄. The DSC curve is shown in Figure 29. The energy release before 600 °C was found to be much greater in air than in argon. The system of Al/CuO nanothermite exhibits the highest heat release with 5125 J·g⁻¹, while Al/Co₃O₄ releases 3958 J·g⁻¹ heat, which is the lowest among the four samples.

Therefore, the nature of the oxidant has an essential influence on the reaction kinetics and reaction mechanism of the thermite composites. Composite MOs could combine the properties of two single MOs with special properties such as electrical conductivity, excellent catalytic activity, and synergistic effect, which may be better than the mixture of two MOs [147,148].

As far as the structure of the composite material is concerned, the uniform distribution and compactness mean that the interfacial contact between the components is close, and the mass transfer and thermal diffusion distances are short, which is very beneficial for promoting the reaction kinetics and improving the performance.

Wang et al. [149] assembled a novel NC coated aluminum/copper ferrite (Al/CuFe₂O₄@NC) thermite using electro spray technique to improve the distribution and enhance the interfacial contact between the components. The thermites with these different oxides were obtained using NC as a binder. The thermal behavior, laser ignition and combustion properties of the assembled Al/CuFe₂O₄@NC were evaluated and compared with their physical mixtures. Compared with Al/CuO@NC and Al/Fe₂O₃@NC composites, Al/CuFe₂O₄@NC composites have lower boost rate and longer duration. Furthermore, the thermites prepared by electro spraying exhibit better properties than the samples by simple physical mixing. Thus, uniform distribution and close interfacial contact of the fuel and the oxidant do much help in enhancing the performance.

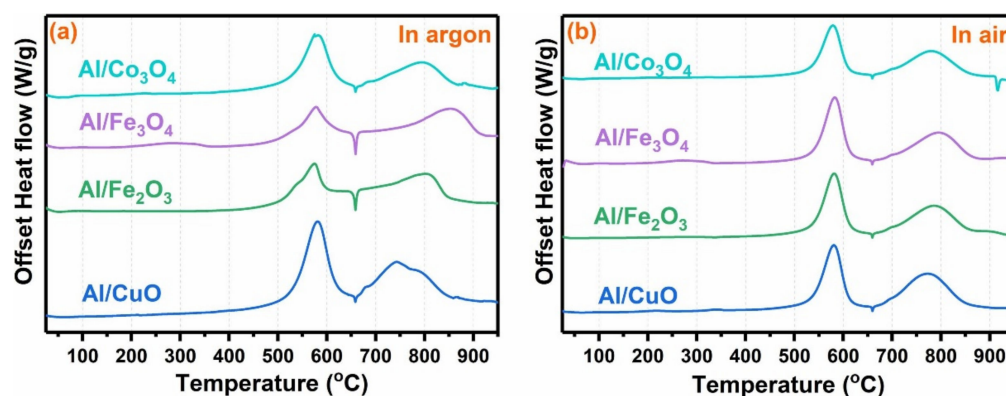


Figure 29. DSC traces collected for Al/CuO, Al/Fe₂O₃, Al/Fe₃O₄ and Al/Co₃O₄ as prepared and ramped in flowing Ar (a) and air (b) at 10 °C/min. The y-axis values are offset. (a,b) Reproduced with the permission of ref. [145]. Copyright 2021, Chemical Engineering Journal.

Further combustion pressure experiment was carried out for exploring the pressurization characteristics of the thermite during the combustion process. Representative time resolved pressure and light emission curves of Al/CuO@NC, Al/Fe₂O₃@NC and Al/CuFe₂O₄@NC composites are shown in Figure 30a,b, respectively. Light emission represents the duration of recombination combustion in the confined combustion chamber. The result indicated that Al/CuO@NC has the largest pressurization rate and the shortest

duration, indicating a vigorous combustion reaction and a high reactivity. As a contrast, the Al/CuFe₂O₄@NC composite has a lower pressing rate and longer duration. Thus, the oxidant can greatly affect the combustion duration and pressurization rate of the composite.

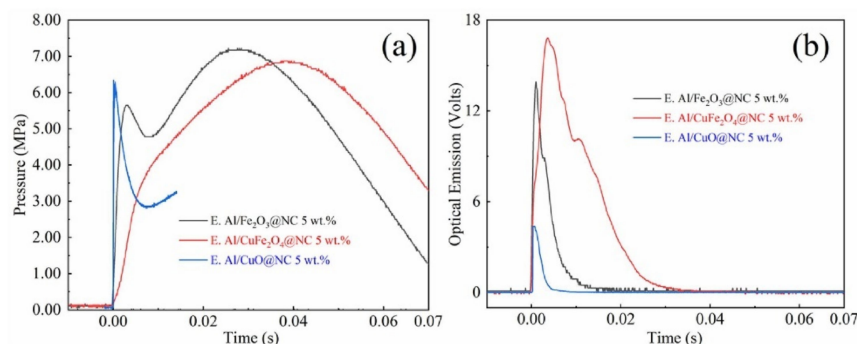


Figure 30. The representative time resolved pressure and optical emission curves of Al/CuO@NC, Al/Fe₂O₃@NC and Al/CuFe₂O₄@NC composites. (a,b) Reproduced with the permission of ref. [149]. Copyright 2022, Fuel.

Shi et al. [150] first prepared monodispersed polystyrene (PS) by an emulsifier-free polymerization method. Then, the macroporous (3DOM) NiFe₂O₄ was obtained through immersing the colloidal crystal template to the methanol and ethylene glycol solution (volume ratio of 1:1) of Fe(NO₃)₃·9H₂O and Ni(NO₃)₂·6H₂O with stirring and the later calcination. The Al/NiFe₂O₄ nanothermite was finally prepared by magnetron sputtering nano-Al to the 3D-DOM NiFe₂O₄ under vacuum. The surface view of the PS template, the honeycomb structure NiFe₂O₄ films and the Al/NiFe₂O₄ were shown in Figure 31. The unique three-dimensional pore structure helps to increase the heat release of the thermite reaction and makes the as-prepared thermite to be easily ignited by laser.

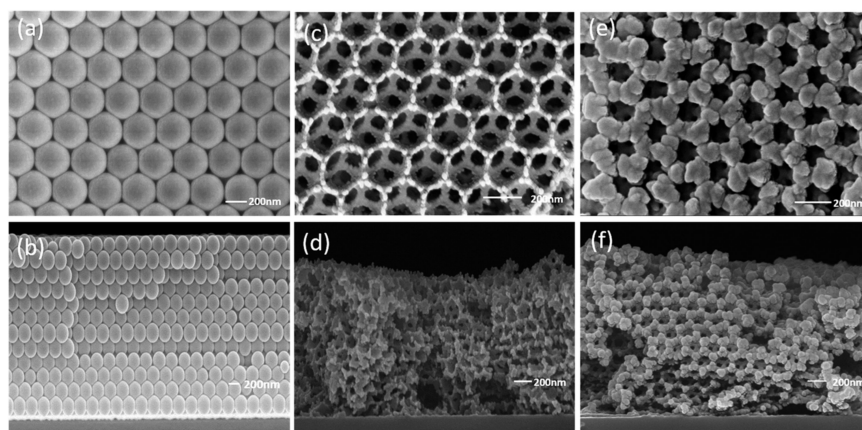


Figure 31. SEM images of (a,b) PS template, (c,d) 3DOM NiFe₂O₄ membrane and (e,f) 3DOM Al/NiFe₂O₄ membrane after Al deposition, (a,c,e) surface view and (b,d,f) cross-section view. (a–f) Reproduced with the permission of ref. [150]. Copyright 2016, RSC Advances.

5.3. Nano-Thermite with Different Morphologies and Their Catalytic Effects on EMs

Al/Fe₂O₃ is a traditional thermite with an energy density of 3.71 kJ·g^{−1} and a reaction temperature of up to 3135 K. It is widely used as propellants and additives for high explosives, airbag ignition materials, welding torches, etc. Fe₂O₃ with different morphologies presents differently in the thermite reaction.

Our group [8] studied the thermite reaction of Al/Fe₂O₃ with three different morphologies which is granular, oval and polyhedral of Fe₂O₃. The SEM images and the DSC curve are shown in Figure 32. The thermite reaction happened before the melting of Al powder when the particle size is micro or nano. Additionally, the thermal process was

quite different among the three thermites. The Al/Fe₂O₃ (granular) particles exhibit one rapid exothermic process under 660 °C, which may attribute to the highest burning rate in AP/HTPB composite propellants.

Yang et al. [151] successfully used the electrospray process to prepare aluminum nanopowder and iron oxide nanopowder Al/Fe₂O₃/RDX/NC composites with different RDX contents. The RDX in the precursor solution plays an important role in the morphology of the composites. After adding RDX to the composite, a loose structure was formed. DSC curves (Figure 33) showed that the decomposition temperature of RDX was reduced by about 20 °C through the electrospray prepared composition compared to RDX. The combustion performance in air showed that RDX reduced the combustion performance of nano-thermite, and the combustion intensity decreased with the increase of RDX content. In addition, the combustion chamber test shows that the maximum pressure peak of the Al/Fe₂O₃/RDX/NC composite is greatly improved.

The addition of AP to the porous network of Al/Fe₂O₃ can generate MICs with uniform density. Gao et al. [152] immersed nano-aluminum particles into the pores of hematite matrix to form Al/Fe₂O₃ nano-thermite through sol-gel processing. Then, porous Al/Fe₂O₃ particles were combined with AP using wet impregnation and solvent-antisolvent techniques. Thus, the MICs-AP/Al/Fe₂O₃ nano-thermite was obtained. The SEM images (Figure 34a) show that AP and nano-aluminum are dispersed in the pores of the hematite gel with a large specific surface area. DSC curves of the AP, AP + Al/Fe₂O₃ and AP/Al/Fe₂O₃ were plotted, as shown in Figure 34b. The Al/Fe₂O₃ nano-thermite plays a catalytic role in the thermal decomposition of AP, and the interaction of the thermite reaction is greatly enhanced by the accelerated decomposition of AP. The activation energy of AP was decreased from 176.84 kJ·mol⁻¹ to 109.22 kJ·mol⁻¹.

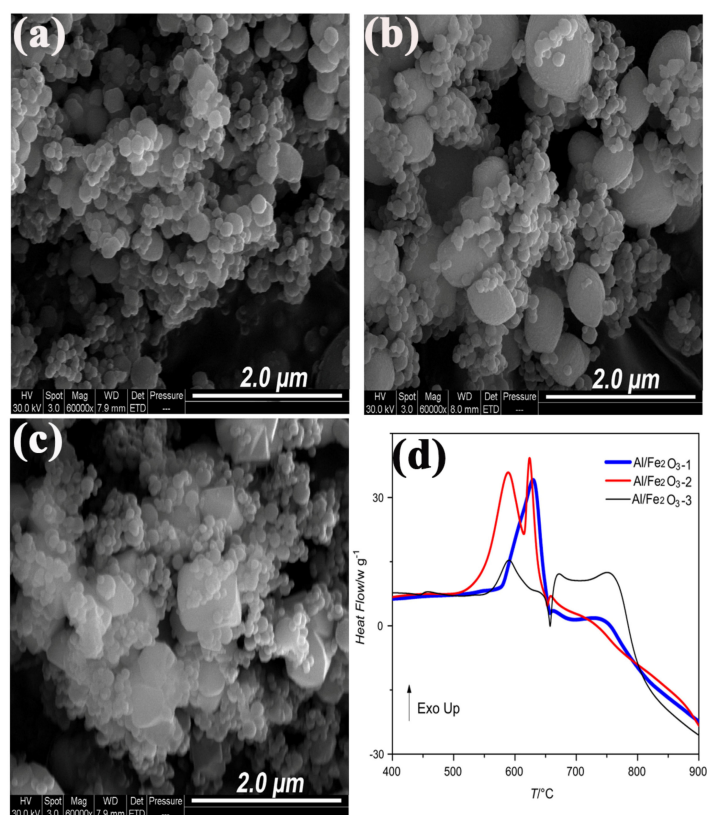


Figure 32. SEM images of (a) Al/Fe₂O₃-granular, (b) Al/Fe₂O₃-oval, (c) Al/Fe₂O₃-polyhedral, (d) DSC curves of the three thermites obtained at a heating rate of 10 °C·min⁻¹ (1-granular, 2-oval, 3-polyhedral). (a–d) Reproduced with the permission of ref. [8]. Copyright 2014, Journal of Solid State Chemistry.

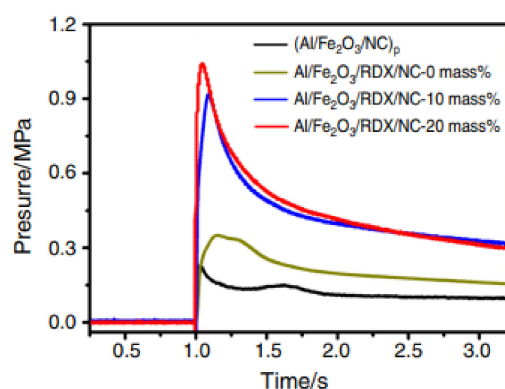


Figure 33. Temporal pressure rise curves during the reaction of $(\text{Al}/\text{Fe}_2\text{O}_3/\text{NC})_p$ composites prepared by simple physical mixing and $\text{Al}/\text{Fe}_2\text{O}_3/\text{RDX}/\text{NC}$ composites containing different RDX contents prepared by electrospray process. Reproduced with the permission of ref. [151]. Copyright 2019, Journal of Thermal Analysis and Calorimetry.

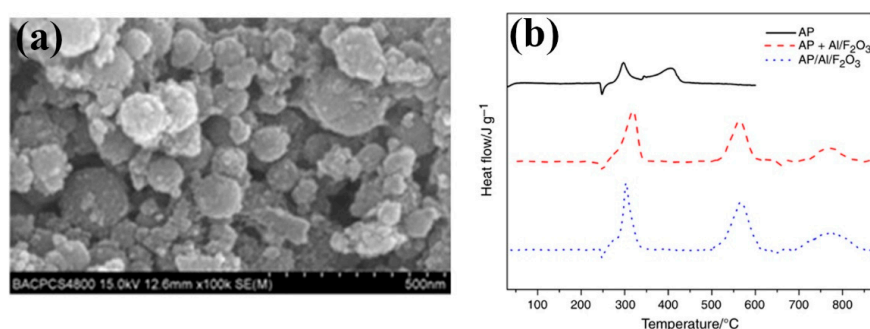


Figure 34. (a) SEM images of $\text{Al}/\text{Fe}_2\text{O}_3$; (b) DSC curves of AP, AP + $\text{Al}/\text{Fe}_2\text{O}_3$, AP/ $\text{Al}/\text{Fe}_2\text{O}_3$ at $10\text{ }^\circ\text{C}\cdot\text{min}^{-1}$. (a,b) Reproduced with the permission of ref. [152]. Copyright 2014, Journal of Thermal Analysis and Calorimetry.

As the main energetic component, RDX is widely used in solid propulsion. However, the influence of nano-thermite $\text{Al}/\text{Fe}_2\text{O}_3$ on the thermal decomposition characteristics of RDX is rarely studied. Our group [153] prepared hollow short rod-like nano- Fe_2O_3 by the hydrothermal method and combined it with nano-Al particles by an ultrasonic dispersion method to prepare super thermite. The SEM images of the rod-like Fe_2O_3 and $\text{Al}/\text{Fe}_2\text{O}_3$ are shown in Figure 35a,b. The effects of the super thermite $\text{Al}/\text{Fe}_2\text{O}_3$ on the thermal decomposition properties of RDX were studied by DSC (Figure 35c). The results show that the addition of nano-thermite changes the thermal decomposition process of RDX and intensifies the secondary gas phase reaction of RDX. With the increase in super thermite content, the peak shape of the decomposition peak of RDX significantly changes. The second shoulder peak temperature for the thermal decomposition peak of RDX decreases.

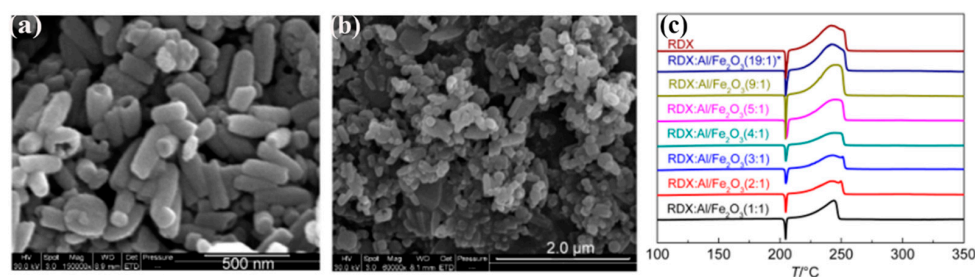


Figure 35. (a,b) SEM images of nano- Fe_2O_3 and super thermite $\text{Al}/\text{Fe}_2\text{O}_3$; (c) DSC curves of RDX and RDX/super thermite ($\text{Al}/\text{Fe}_2\text{O}_3$) mixture. (a–c) Reproduced with the permission of ref. [153]. Copyright 2013, Acta Physico-Chimica Sinica.

Furthermore, our group [154] used $\text{FeCl}_3 \cdot 6\text{H}_2\text{O}$ and NaOH as raw materials to prepare rod-like Fe_2O_3 by a hydrothermal synthesis method at $180\text{ }^\circ\text{C}$ for 6 h. Another two Fe_2O_3 nano-particles with olivary and polyhedral morphologies were also prepared. Then, $\text{Al}/\text{Fe}_2\text{O}_3/\text{NC}$ composites were designed and fabricated using various morphologies of Fe_2O_3 . The TEM images of the three samples with different morphologies were shown in Figure 36. The effect of $\text{Al}/\text{Fe}_2\text{O}_3$ on the thermal decomposition properties of NC was studied in detail by DSC (Figure 37). Compared with other morphological samples, the performance of $\text{Al}/\text{Fe}_2\text{O}_3$ containing rod-like Fe_2O_3 is greatly improved. The E_a and thermal ignition temperature (T_{beo}) of $\text{Al}/\text{r-Fe}_2\text{O}_3/\text{NC}$ are the lowest.

Recently, 3D printing techniques raise much interest in composite preparation. MICs inks for thermite is a challenging work. Zhong et al. [155] used a core-shell nozzle for 3D printing to prepare $\text{Al}/\text{Fe}_2\text{O}_3/\text{F2311}$ thermite using 15% (wt%) fluororubber (F2311) as polymer binder (Figure 38a). The 3D printing technique ensures that the formulations all have hollow uniform filaments with a constant diameter of $\sim 0.5\text{ mm}$. DSC results (Figure 38b) show that the onset thermal decomposition temperature of $\text{Al}/\text{Fe}_2\text{O}_3/\text{F2311}$ is $368\text{ }^\circ\text{C}$, and the heat release is $1552\text{ J}\cdot\text{g}^{-1}$.

Table 4 summarizes the relevant parameters such as their preparation methods and applications of thermite. Al is the most commonly used fuel in composite solid propellants, the oxidizing agent in the aluminothermic composite has a significant effect on the energy release, ignition delay and combustion performance. The uniform distribution and tight interfacial contact between fuel and oxidant is beneficial to shorten the distance for mass transfer and thermal diffusion, thus enhancing the performance of thermites.

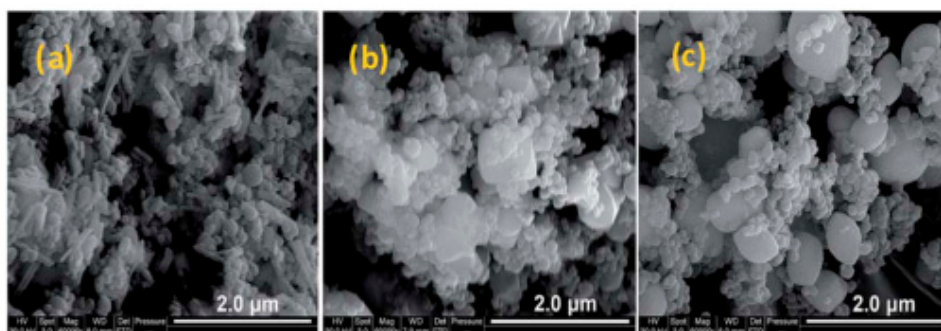


Figure 36. SEM images of $\text{Al}/\text{Fe}_2\text{O}_3$. (a) $\text{Al}/\text{Fe}_2\text{O}_3$ (r); (b) $\text{Al}/\text{Fe}_2\text{O}_3$ (p) and (c) $\text{Al}/\text{Fe}_2\text{O}_3$ (o). (a–c) Reproduced with the permission of ref. [154]. Copyright 2017, RSC Advances.

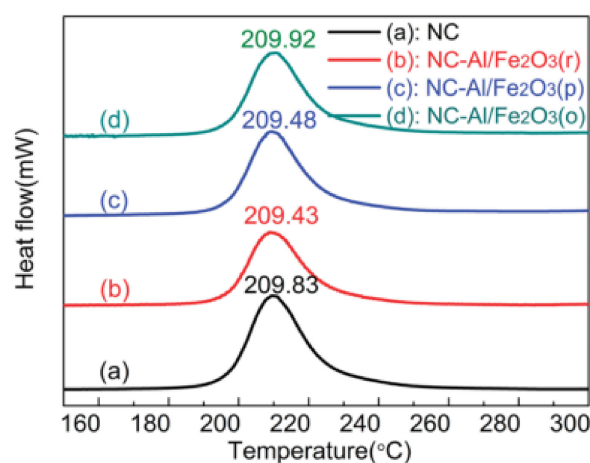


Figure 37. DSC curves of $\text{NC-}\text{Al}/\text{Fe}_2\text{O}_3$ and NC . Reproduced with the permission of ref. [154]. Copyright 2017, RSC Advances.

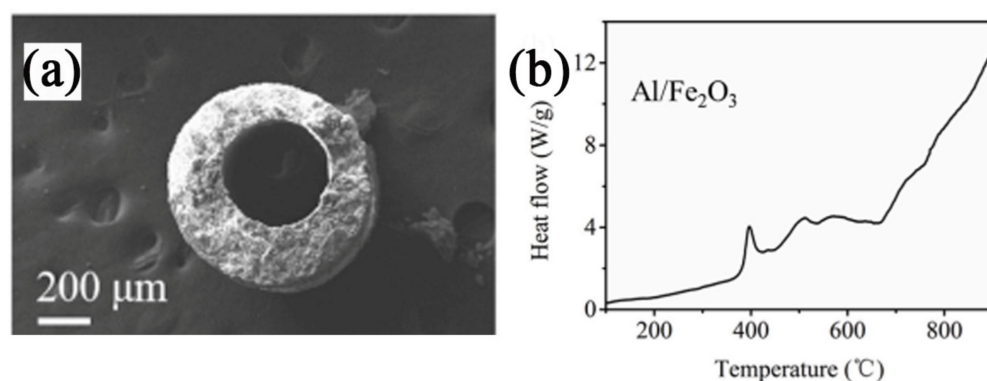


Figure 38. (a) SEM images of Al/Fe₂O₃/F2311; (b) DSC curves of Al/Fe₂O₃/F2311. (a,b) Reproduced with the permission of ref. [155]. Copyright 2021, Materials Chemistry and Physics.

Table 4. Parameters of some nano-thermites.

Materials	Preparation Method	Application	T_{exo1}	T_{exo2}	ΔH	Ref.
Al/B/Fe ₂ O ₃	sol-gel synthetic	thermite	582.0	790.0	3270.0	[133]
Al/B/Fe ₂ O ₃	physical blending		559.0	780.0	2610.0	
Al/Fe ₂ O ₃	one-step hydrothermal	solid propellants	587.0 ± 1.0	785.0 ± 2.0	3125.0 ± 31.0	[134]
Al/Bi _{0.1} -Fe ₂ O ₃			602.0 ± 2.0	727.0 ± 8.0	2893.0 ± 16.0	
Al/Bi _{0.2} -Fe ₂ O ₃			597.0 ± 1.0	696.0 ± 5.0	2720.0 ± 22.0	
Al/Bi _{0.3} -Fe ₂ O ₃			593.0 ± 2.0	684.0 ± 3.0	2349.0 ± 14.0	
Al/Bi ₂ O ₃			574.0 ± 10.0	667.0 ± 13.0	852.0 ± 34.0	
Al/BiFeO ₃			583.0 ± 1.0	739.0 ± 2.0	1812.0 ± 23.0	
in Ar Al/CuO	virtual thermal aging	thermite	528.0	691.0	3945.0	
in Ar Al/Fe ₂ O ₃			514.0	733.0	2791.0	[145]
in Ar Al/Fe ₃ O ₄			527.0	770.0	2516.0	
in Ar Al/Co ₃ O ₄			534.0	698.0	2457.0	
in air Al/CuO			538.0	697.0	5125.0	
in air Al/Fe ₂ O ₃			539.0	705.0	4214.0	
in air Al/Fe ₃ O ₄			540.0	710.0	4302.0	
in air Al/Co ₃ O ₄			536.0	702.0	3958.0	
Al/CuFe ₂ O ₄ @NC	electrospray		567.8	-	2064.6	[149]
Al/Fe ₂ O ₃ @NC 5wt%			576.5	-	2348.5	
Al/Cuo@NC 5wt%			598.8	-	1763.9	
Al/NiFe ₂ O ₄	templating	MEMS	359.2	594.6	2921.7	[150]
Al/Fe ₂ O ₃ /NC	electrospray	pyrotechnics	201.4	587.8	-	[151]
Al/Fe ₂ O ₃ /RDX/NC-0		thermite	206.2	589.6	-	
Al/Fe ₂ O ₃ /RDX/NC-10			224.7	581.8	-	
Al/Fe ₂ O ₃ /RDX/NC-20			227.7	584.6	-	
Al/Fe ₂ O ₃ +AP	physicalmixing	micro-propellants	-	-	1820.0	[152]
Al/Fe ₂ O ₃ /AP	solvent-anti-solvent		-	-	1400.0	
Al/Fe ₂ O ₃ /RDX (1:19)	hydrothermal	super thermites	241.6	-	-	[153]
Al/Fe ₂ O ₃ /RDX (1:9)			246.3	-	-	
Al/Fe ₂ O ₃ /RDX (1:5)			246.0	-	-	
Al/Fe ₂ O ₃ /RDX (1:4)			245.9	-	-	
Al/Fe ₂ O ₃ /RDX (1:3)			242.5	250.9	-	
Al/Fe ₂ O ₃ /RDX (1:2)			239.6	247.2	-	
Al/Fe ₂ O ₃ /RDX (1:1)			244.5	-	-	
Al/Fe ₂ O ₃ (p)/NC	hydrothermal	micro-propellants	209.5	-	-	[154]
Al/Fe ₂ O ₃ (o)/NC			209.9	-	-	
Al/Fe ₂ O ₃ (r)/NC			209.4	-	-	
Al/CuO/F2311	3D printing		288.0	-	1500.0	
Al/Fe ₂ O ₃ /F2311			368.0	-	1552.0	
Al/Bi ₂ O ₃ /F2311			410.0	-	1071.0	
Al/PtFE/F2311			377.0	-	7200.0	

Note: T_{exo1} is the first exothermic temperature(°C); T_{exo2} is the second exothermic temperature(°C); ΔH is the energy output ($\text{J}\cdot\text{g}^{-1}$).

Different kinds of thermites like Al/KMnO₄, Al/SnO and Al/AgIO₃ are prepared to meet different applications. The fabrication methods include some new techniques such as vapor deposition, high-energy ball milling, electrophoretic deposition, etc. [156]. With the

development of preparation methods and techniques, the thermite will be more specific and multifunctional.

6. Future Outlook

The preparation of hematite with different morphologies and their enhanced effect on the thermal decomposition of AP, RDX, HMX, CL-20, etc., were summarized. The morphology has been proved to be able to greatly affect the thermal decomposition behavior of EMs. Making ferrite, combined with some carbon materials, can promote the catalytic effect of hematite because more active spots were supplied. GO was a good carrier of the catalyst which can effectively decrease the aggregated degree of the nano metal oxide particles. The g-C₃N₄ raised much attention as a two-dimension carbon material. When combining hematite with nano-sized Al powder to make the super-thermite, the composite can release more energy and exhibit good catalytic effects on EMs. With the development of material and preparation techniques, more new hematite formulations will be explored, the performances of EMs will be enhanced. The application of hematite in EMs still needs long term research and exploration. The combination of carbon materials with high specific surface area or porous structure can greatly help to solve the problems of poor dispersion in thermite preparation and energetic composites. Thereby enhancing the properties of hematite or hematite composites.

Author Contributions: Conceptualization, Y.L. and J.D.; methodology, Y.M.; validation, Y.M.; resources, Y.L.; data curation, J.D.; writing—original draft preparation, Y.L.; writing—review and editing, Y.L. and H.M.; supervision, H.M. All authors have read and agreed to the published version of the manuscript.

Funding: This research was funded by the Shaanxi Key Science and Technology Innovation Team Project (2022TD-33) and the Program for the National Natural Science Foundation of China (No. 21373161).

Institutional Review Board Statement: Not applicable.

Informed Consent Statement: Not applicable.

Data Availability Statement: Not applicable.

Acknowledgments: This work was supported by Shaanxi Key Science and Technology Innovation Team Project (2022TD-33) and the Program for the National Natural Science Foundation of China (No. 21373161).

Conflicts of Interest: The authors declare no conflict of interest.

References

1. Chen, L.; Li, F.; Ni, B.B.; Xu, J.; Fu, Z.P.; Lu, Y.L. Enhanced visible photocatalytic activity of hybrid Pt/ α -Fe₂O₃ nanorods. *RSC Adv.* **2012**, *2*, 10057–10063. [[CrossRef](#)]
2. Eggleston, C.M. Toward new uses for hematite. *Science* **2008**, *320*, 184–185. [[CrossRef](#)]
3. Sakurai, S.; Namai, A.; Hashimoto, K.; Ohkoshi, S. First Observation of Phase Transformation of All Four Fe₂O₃ Phases ($\gamma \rightarrow \epsilon \rightarrow \beta \rightarrow \alpha$ -Phase). *J. Am. Chem. Soc.* **2009**, *131*, 18299–18303. [[CrossRef](#)]
4. Ando, M.; Kadono, K.; Haruta, M.; Sakaguchi, T.; Miya, M. Large third-order optical nonlinearities in transition-metal oxides. *Nature* **1995**, *374*, 625–627. [[CrossRef](#)]
5. Sun, B.; Horvat, J.; Kim, H.S.; Kim, W.S.; Ahn, J.; Wang, G.X. Synthesis of Mesoporous α -Fe₂O₃ Nanostructures for Highly Sensitive Gas Sensors and High Capacity Anode Materials in Lithium Ion Batteries. *J. Phys. Chem. C* **2010**, *114*, 18753–18761. [[CrossRef](#)]
6. Reddy, M.V.; Yu, T.; Sow, C.H.; Shen, Z.X.; Lim, C.T.; Rao, G.V.S.; Chowdari, B.V.R. α -Fe₂O₃ nanoflakes as an anode material for Li-ion batteries. *Adv. Funct. Mater.* **2007**, *17*, 2792–2799. [[CrossRef](#)]
7. Zhong, L.S.; Hu, J.S.; Liang, H.P.; Cao, A.M.; Song, W.G.; Wan, L.J. Self-assembled 3D flowerlike iron oxide nanostructures and their application in water treatment. *Adv. Mater.* **2006**, *18*, 2426–2431. [[CrossRef](#)]
8. Zhao, N.N.; He, C.C.; Liu, J.B.; Gong, H.J.; An, T.; Xu, H.X.; Zhao, F.Q.; Hu, R.Z.; Ma, H.X.; Zhang, J.Z. Dependence of catalytic properties of Al/Fe₂O₃ thermites on morphology of Fe₂O₃ particles in combustion reactions. *J. Solid State Chem.* **2014**, *219*, 67–73. [[CrossRef](#)]

9. Ling, Y.C.; Wang, G.M.; Reddy, J.; Wang, C.C.; Zhang, J.Z.; Li, Y. The Influence of Oxygen Content on the Thermal Activation of Hematite Nanowires. *Angew. Chem. Int. Ed. Engl.* **2012**, *51*, 4074–4079. [[CrossRef](#)] [[PubMed](#)]
10. Zhao, N.N. Research on the Preparation, Properties and Application of Micro-Nano Metal Oxides and Thermite in Composite Propellants. Ph.D. Thesis, Northwest University, Xi'an, China, 2015.
11. Larcher, D.; Bonnin, D.; Cortes, R.; Rivals, I.; Personnaz, L.; Tarascon, J.M. Combined XRD, EXAFS, and Mossbauer studies of the reduction by lithium of alpha-Fe₂O₃ with various particle sizes. *J. Electrochem. Soc.* **2003**, *150*, A1643–A1650. [[CrossRef](#)]
12. Xue, D.S.; Gao, C.X.; Liu, Q.F.; Zhang, L.Y. Preparation and characterization of haematite nanowire arrays. *J. Phys. Condens. Matter* **2003**, *15*, 1455–1459. [[CrossRef](#)]
13. Jia, C.J.; Sun, L.D.; Yan, Z.G.; You, L.P.; Luo, F.; Han, X.D.; Pang, Y.C.; Zhang, Z.; Yan, C.H. Iron oxide nanotubes—Single-crystalline iron oxide nanotubes. *Angew. Chem. Int. Ed.* **2005**, *44*, 4328–4333. [[CrossRef](#)]
14. Jia, C.J.; Sun, L.D.; Luo, F.; Han, X.D.; Heyderman, L.J.; Yan, Z.G.; Yan, C.H.; Zheng, K.; Zhang, Z.; Takano, M.; et al. Large-Scale Synthesis of Single-Crystalline Iron Oxide Magnetic Nanorings. *J. Am. Chem. Soc.* **2008**, *130*, 16968–16977. [[CrossRef](#)] [[PubMed](#)]
15. Eltschka, M.; Klaui, M.; Ruediger, U.; Kasama, T.; Cervera-Gontard, L.; Dunin-Borkowski, R.E.; Luo, F.; Heyderman, L.J.; Jia, C.J.; Sun, L.D.; et al. Correlation between magnetic spin structure and the three-dimensional geometry in chemically synthesized nanoscale magnetite rings. *Appl. Phys. Lett.* **2008**, *92*, 222508. [[CrossRef](#)]
16. Uhm, Y.R.; Kim, W.W.; Rhee, C.K. A study of synthesis and phase transition of nanofibrous Fe₂O₃ derived from hydrolysis of Fe nanopowders. *Scr. Mater.* **2004**, *50*, 561–564. [[CrossRef](#)]
17. Li, L.L.; Chu, Y.; Liu, Y.; Dong, L.H. Template-free synthesis and photocatalytic properties of novel, Fe₂O₃ hollow spheres. *J. Phys. Chem. C* **2007**, *111*, 2123–2127. [[CrossRef](#)]
18. Wen, X.G.; Wang, S.H.; Ding, Y.; Wang, Z.L.; Yang, S.H. Controlled growth of large-area, uniform, vertically aligned arrays of alpha-Fe₂O₃ nanobelts and nanowires. *J. Phys. Chem. B* **2005**, *109*, 215–220. [[CrossRef](#)] [[PubMed](#)]
19. Zeng, S.Y.; Tang, K.B.; Li, T.W.; Liang, Z.H.; Wang, D.; Wang, Y.K.; Qi, Y.X.; Zhou, W.W. Facile route for the fabrication of porous hematite nanoflowers: Its synthesis, growth mechanism, application in the lithium ion battery, and magnetic and photocatalytic properties. *J. Phys. Chem. C* **2008**, *112*, 4836–4843. [[CrossRef](#)]
20. Gotic, M.; Drazic, G.; Music, S. Hydrothermal synthesis of alpha-Fe₂O₃ nanorings with the help of divalent metal cations, Mn²⁺, Cu²⁺, Zn²⁺ and Ni²⁺. *J. Mol. Struct.* **2011**, *993*, 167–176. [[CrossRef](#)]
21. Lv, B.L.; Xu, Y.; Wu, D.; Sun, Y.H. Single-crystal alpha-Fe₂O₃ hexagonal nanorings: Stepwise influence of different anionic ligands (F⁻ and SCN⁻ anions). *Chem. Commun.* **2011**, *47*, 967–969. [[CrossRef](#)]
22. Lv, B.L.; Xu, Y.; Wu, D.; Sun, Y.H. Modification Effect of SCN⁻ Ions on the Morphology of alpha-Fe₂O₃ Nanoparticles. *Chem. Lett.* **2008**, *37*, 1152–1153. [[CrossRef](#)]
23. Zhang, X.L.; Sui, C.H.; Gong, J.; Su, Z.M.; Qu, L.Y. Preparation and formation mechanism of different alpha-Fe₂O₃ morphologies from snowflake to paired microplates, dumbbell, and spindle microstructures. *J. Phys. Chem. C* **2007**, *111*, 9049–9054. [[CrossRef](#)]
24. Tian, N.; Zhou, Z.-Y.; Sun, S.-G.; Ding, Y.; Wang, Z.L. Synthesis of tetrahedral platinum nanocrystals with high-index facets and high electro-oxidation activity. *Science* **2007**, *316*, 732–735. [[CrossRef](#)] [[PubMed](#)]
25. Jeong, G.H.; Kim, M.; Lee, Y.W.; Choi, W.; Oh, W.T.; Park, Q.H.; Han, S.W. Polyhedral Au Nanocrystals Exclusively Bound by {110} Facets: The Rhombic Dodecahedron. *J. Am. Chem. Soc.* **2009**, *131*, 1672–1673. [[CrossRef](#)]
26. Ma, Y.Y.; Kuang, Q.; Jiang, Z.Y.; Xie, Z.X.; Huang, R.B.; Zheng, L.S. Synthesis of Trisoctahedral Gold Nanocrystals with Exposed High-Index Facets by a Facile Chemical Method. *Angew. Chem. Int. Ed.* **2008**, *47*, 8901–8904. [[CrossRef](#)]
27. Zhang, J.; Sasaki, K.; Sutter, E.; Adzic, R.R. Stabilization of platinum oxygen-reduction electrocatalysts using gold clusters. *Science* **2007**, *315*, 220–222. [[CrossRef](#)]
28. Stamenkovic, V.R.; Fowler, B.; Mun, B.S.; Wang, G.; Ross, P.N.; Lucas, C.A.; Markovic, N.M. Improved oxygen reduction activity on Pt₃Ni(111) via increased surface site availability. *Science* **2007**, *315*, 493–497. [[CrossRef](#)]
29. Narayanan, R.; El-Sayed, M.A. Shape-dependent catalytic activity of platinum nanoparticles in colloidal solution. *Nano Lett.* **2004**, *4*, 1343–1348. [[CrossRef](#)]
30. Vidal-Iglesias, F.J.; Solla-Gullon, J.; Rodriguez, P.; Herrero, E.; Montiel, V.; Feliu, J.M.; Aldaz, A. Shape-dependent electrocatalysis: Ammonia oxidation on platinum nanoparticles with preferential (100) surfaces. *Electrochem. Commun.* **2004**, *6*, 1080–1084. [[CrossRef](#)]
31. Yin, J.Z. Synthesis of Functional Nanostructures Assisted by Cellulose-based Polymeric Surfactants. Ph.D. Thesis, Nanjing University, NanKing, China, 2011.
32. Ma, H.X.; Zhao, N.N.; Zhao, F.Q. *Nano-Metal Oxides and Super-Thermite*; Science Press: Beijing, China, 2022.
33. Jiao, H.; Yang, H. Thermal decomposition synthesis of 3D urchin-like alpha-Fe₂O₃ superstructures. *Mater. Sci. Eng. B Adv. Funct. Solid State Mater.* **2009**, *156*, 68–72.
34. Lv, B.L.; Liu, Z.Y.; Tian, H.; Xu, Y.; Wu, D.; Sun, Y.H. Single-Crystalline Dodecahedral and Octodecahedral alpha-Fe₂O₃ Particles Synthesized by a Fluoride Anion-Assisted Hydrothermal Method. *Adv. Funct. Mater.* **2010**, *20*, 3987–3996. [[CrossRef](#)]
35. Lv, B.L.; Zhou, H.; Wu, D.; Xu, Y. Single-crystalline dodecahedral alpha-Fe₂O₃ particles with nanometer size: Synthesis and characterization. *J. Nanopart. Res.* **2014**, *16*, 2799. [[CrossRef](#)]
36. Xu, H.; Wang, X.; Zhang, L. Selective preparation of nanorods and micro-octahedrons of Fe₂O₃ and their catalytic performances for thermal decomposition of ammonium perchlorate. *Powder Technol.* **2008**, *185*, 176–180. [[CrossRef](#)]

37. Yang, Y.; Ma, H.; Zhuang, J.; Wang, X. Morphology-Controlled Synthesis of Hematite Nanocrystals and Their Facet Effects on Gas-Sensing Properties. *Inorg. Chem.* **2011**, *50*, 10143–10151. [[CrossRef](#)] [[PubMed](#)]
38. Gao, R.; Zhao, N.N.; Liu, J.B.; Zhang, T.; Ma, H.X. Catalytic Effect of Two Shapes of Nano-Fe₂O₃ on Hexanitrohexaazaisowurtzitane Using a Non-Isothermal Decomposition Kinetic Method. *Propellants Explos. Pyrotech.* **2016**, *41*, 936–941. [[CrossRef](#)]
39. Benhameda, A.; Trache, D.; Kesraoui, M.; Tarchoun, A.F.; Chelouche, S.; Mezroua, A. Synthesis and characterization of alpha-Fe₂O₃ nanoparticles from different precursors and their catalytic effect on the thermal decomposition of nitrocellulose. *Thermochim. Acta* **2020**, *686*, 178570. [[CrossRef](#)]
40. Zhao, N.N.; Li, J.C.; Gong, H.J.; An, T.; Zhao, F.Q.; Yang, A.W.; Hu, R.Z.; Ma, H.X. Effects of alpha-Fe₂O₃ nanoparticles on the thermal behavior and non-isothermal decomposition kinetics of nitrocellulose. *J. Anal. Appl. Pyrolysis* **2016**, *120*, 165–173. [[CrossRef](#)]
41. Elbasuney, S.; Yehia, M.; Hamed, A.; Ismael, S.; Mokhtar, M.; Elsaka, E.; Gobara, M.; Saleh, A.; El-Sayyad, G.S. Ferric oxide colloid: Novel nanocatalyst for heterocyclic nitramines. *J. Mater. Sci. Mater. Electron.* **2021**, *32*, 4185–4195. [[CrossRef](#)]
42. Zhang, Y.; Xu, G.; Ou, P.; Han, G.-R. Preparation and catalytic property of single crystal multiporous alpha-Fe₂O₃ nanorods. *J. Inorg. Mater.* **2008**, *23*, 459–463. [[CrossRef](#)]
43. Zhou, L.Y.; Cao, S.B.; Zhang, L.L.; Xiang, G.; Zeng, X.F.; Chu, G.W.; Chen, J.F. Quantitatively evaluating activity and number of catalytic sites on metal oxide for ammonium perchlorate decomposition. *AIChE J.* **2022**, *68*, 17582. [[CrossRef](#)]
44. Shi, S.H.; Xu, G. Uniform hematite hexagonal nanodisks with dominant (001) facets: Hydrothermal synthesis and catalytic performance for the decomposition of ammonium perchlorate. *Appl. Mech. Mater.* **2014**, *651–653*, 161–164. [[CrossRef](#)]
45. Sharma, J.K.; Srivastava, P.; Akhtar, M.S.; Singh, G.; Ameen, S. alpha-Fe₂O₃ hexagonal cones synthesized from the leaf extract of *Azadirachta indica* and its thermal catalytic activity. *New J. Chem.* **2015**, *39*, 7105–7111. [[CrossRef](#)]
46. Cao, S.B.; Han, X.G.; Zhang, L.L.; Wang, J.X.; Luo, Y.; Zou, H.K.; Chen, J.F. Facile and scalable preparation of alpha-Fe₂O₃ nanoparticle by high-gravity reactive precipitation method for catalysis of solid propellants combustion. *Powder Technol.* **2019**, *353*, 444–449. [[CrossRef](#)]
47. Li, C.C.; Zhang, T.; An, J.; Zeng, J.; Ma, H.X. Research progress of three-dimensional ordered macroporous perovskite metal oxides as highly efficient combustion catalysts. *Chem. Ind. Eng. Prog.* **2021**, *40*, 3181–3190.
48. Wu, Q.Z.; Li, Y.G. Progress of applications of three-dimensionally ordered macroporous materials. *Chem. Ind. Eng. Prog.* **2008**, *27*, 358–363.
49. Tanaka, H.; Misono, M. Advances in designing perovskite catalysts. *Curr. Opin. Solid State Mater. Sci.* **2001**, *5*, 381–387. [[CrossRef](#)]
50. Crespin, M.; Hall, W.K. The surface chemistry of some perovskite oxides. *J. Catal.* **1981**, *69*, 359–370. [[CrossRef](#)]
51. Humayun, M.; Ullah, H.; Usman, M.; Habibi-Yangjeh, A.; Tahir, A.A.; Wang, C.D.; Luo, W. Perovskite-type lanthanum ferrite based photocatalysts: Preparation, properties, and applications. *J. Energy Chem.* **2022**, *66*, 314–338. [[CrossRef](#)]
52. Shi, J.W.; Guo, L.J. ABO₃-based photocatalysts for water splitting. *Prog. Nat. Sci. Mater. Int.* **2012**, *22*, 592–615. [[CrossRef](#)]
53. Thirumalairajan, S.; Girija, K.; Ganesh, I.; Mangalaraj, D.; Viswanathan, C.; Balamurugan, A.; Ponpandian, N. Controlled synthesis of perovskite LaFeO₃ microsphere composed of nanoparticles via self-assembly process and their associated photocatalytic activity. *Chem. Eng. J.* **2012**, *209*, 420–428. [[CrossRef](#)]
54. Shen, S.T.; Weng, H.S. Comparative Study of Catalytic Reduction of Nitric Oxide with Carbon Monoxide over the La_{1-x}Sr_xBO₃ (B=Mn, Fe, Co, Ni) Catalysts. *Ind. Eng. Chem. Res.* **1998**, *37*, 2654–2661. [[CrossRef](#)]
55. Belessi, V.C.; Trikalitis, P.N.; Ladavos, A.K.; Bakas, T.V.; Pomonis, P.J. Structure and catalytic activity of La_{1-x}FeO₃ system (x = 0.00, 0.05, 0.10, 0.15, 0.20, 0.25, 0.35) for the NO+CO reaction. *Appl. Catal. A Gen.* **1999**, *177*, 53–68. [[CrossRef](#)]
56. Li, J.; Si, F. Study on Modification Technology of the Combustion Property of the NEPE Propellant. *Energetic Mater.* **2002**, *10*, 4–9.
57. Wei, Z.X.; Xu, Y.Q.; Liu, H.Y.; Hu, C.W. Preparation and catalytic activities of LaFeO₃ and Fe₂O₃ for HMX thermal decomposition. *J. Hazard. Mater.* **2009**, *165*, 1056–1061. [[CrossRef](#)] [[PubMed](#)]
58. Wang, Y.P.; Yang, X.J.; Lu, L.D.; Wang, X. Experimental study on preparation of LaMO₃ (M = Fe, Co, Ni) nanocrystals and their catalytic activity. *Thermochim. Acta* **2006**, *443*, 225–230. [[CrossRef](#)]
59. Zhang, T.; Guo, Y.; Li, C.C.; Li, Y.Y.; Li, J.C.; Zhao, F.Q.; Ma, H.X. The effect of LaFeO₃@MnO₂ on the thermal behavior of energetic compounds: An efficient catalyst with core-shell structure. *Adv. Powder Technol.* **2020**, *31*, 4510–4516. [[CrossRef](#)]
60. Chikazumi, S. *Physics of Ferromagnetism (International Series of Monographs on Physics)*; Oxford University Press Inc.: New York, NY, USA, 2009.
61. Goldman, A. *Modern Ferrite Technology*; Springer: Berlin/Heidelberg, Germany, 2006.
62. Cornell, R.M.; Schwertmann, U. *The Iron Oxides: Structure, Properties, Reactions, Occurrences and Uses*; Wiley-VCH Verlag GmbH & Co. KGaA: Weinheim, Germany, 2003.
63. Long, N.V.; Yang, Y.; Teranishi, T.; Thi, C.M.; Cao, Y.Q.; Nogami, M. Synthesis and magnetism of hierarchical iron oxide particles. *Mater. Des.* **2015**, *86*, 797–808. [[CrossRef](#)]
64. Yuan, C.; Wu, H.B.; Xie, Y.; Lou, X.W. Mixed Transition-Metal Oxides: Design, Synthesis, and Energy-Related Applications. *Angew. Chem. Int. Ed.* **2014**, *53*, 1488–1504. [[CrossRef](#)]
65. Abbas, M.; Islam, M.N.; Rao, B.P.; Aitah, K.E.A.; Kim, C. Facile approach for synthesis of high moment Fe/ferrite and FeCo/ferrite core/shell nanostructures. *Mater. Lett.* **2015**, *139*, 161–164. [[CrossRef](#)]
66. Maaz, K.; Mumtaz, A.; Hasanain, S.K.; Ceylan, A. Synthesis and magnetic properties of cobalt ferrite (CoFe₂O₄) nanoparticles prepared by wet chemical route. *J. Magn. Magn. Mater.* **2007**, *308*, 289–295. [[CrossRef](#)]

67. Long, N.V.; Yang, Y.; Yuasa, M.; Minh, T.C.; Cao, Y.; Nann, T.; Nogami, M. Controlled synthesis and characterization of iron oxide nanostructures with potential applications for gas sensors and the environment. *RSC Adv.* **2014**, *4*, 6383–6390. [[CrossRef](#)]
68. Zhao, H.; Sun, X.; Mao, C.; Du, J. Preparation and microwave-absorbing properties of NiFe₂O₄-polystyrene composites. *Phys. B Condens. Matter* **2009**, *404*, 69–72. [[CrossRef](#)]
69. Rodenas, L.A.G.; Blesa, M.A.; Morando, P.J. Reactivity of metal oxides: Thermal and photochemical dissolution of MO and MFe₂O₄ (M = Ni, Co, Zn). *J. Solid State Chem.* **2008**, *181*, 2350–2358. [[CrossRef](#)]
70. Zu, Y.; Zhang, Y.; Xu, K.; Zhao, F.Q. A graphene oxide-MgWO₄ nanocomposite as an efficient catalyst for the thermal decomposition of RDX, HMX. *RSC Adv.* **2016**, *6*, 31046–31052. [[CrossRef](#)]
71. Fu, Y.; Wang, X. Magnetically Separable ZnFe₂O₄-Graphene Catalyst and its High Photocatalytic Performance under Visible Light Irradiation. *Ind. Eng. Chem. Res.* **2011**, *50*, 7210–7218. [[CrossRef](#)]
72. Zu, Y.; Zhao, Y.; Xu, K.; Tong, Y.; Zhao, F. Preparation and comparison of catalytic performance for nano MgFe₂O₄, GO-loaded MgFe₂O₄ and GO-coated MgFe₂O₄ nanocomposites. *Ceram. Int.* **2016**, *42*, 18844–18850. [[CrossRef](#)]
73. Xiong, W.H.; Zhang, W.C.; Yu, C.P.; Shen, R.Q.; Cheng, J.; Ye, J.H.; Qin, Z.C. Preparation of Nanoporous CoFe₂O₄ and Its Catalytic Performance during the Thermal Decomposition of Ammonium Perchlorate. *Acta Phys. Chim. Sin.* **2016**, *32*, 2093–2100. [[CrossRef](#)]
74. Han, A.; Liao, J.; Ye, M.; Li, Y.; Peng, X. Preparation of Nano-MnFe₂O₄ and Its Catalytic Performance of Thermal Decomposition of Ammonium Perchlorate. *Chin. J. Chem. Eng.* **2011**, *19*, 1047–1051. [[CrossRef](#)]
75. Xiao, X.; Zhang, G.; Wang, Z.; Zhu, Y.; Yan, Z.; Wang, Y. Porous cobaltate: Structure, active sites, thermocatalytic properties for ammonium perchlorate decomposition. *J. Alloys Compd.* **2022**, *908*, 164624. [[CrossRef](#)]
76. Li, Y.; Li, C.; Zeng, J.; Zhang, T.; Li, J.; Guo, Z.; Qin, Z.; Yi, J.; Zhao, F.; Ma, H. Enhanced catalytic activity and ignition characteristics of three-dimensional ordered macroporous FeCo₂O₄ through controlled synthesis. *Adv. Powder Technol.* **2022**, *33*, 103799. [[CrossRef](#)]
77. Liu, T.; Wang, L.; Yang, P.; Hu, B. Preparation of nanometer CuFe₂O₄ by auto-combustion and its catalytic activity on the thermal decomposition of ammonium perchlorate. *Mater. Lett.* **2008**, *62*, 4056–4058. [[CrossRef](#)]
78. Abazari, R.; Mahjoub, A.R. Potential Applications of Magnetic β-AgVO₃/ZnFe₂O₄ Nanocomposites in Dyes, Photocatalytic Degradation, and Catalytic Thermal Decomposition of Ammonium Perchlorate. *Ind. Eng. Chem. Res.* **2017**, *56*, 623–634. [[CrossRef](#)]
79. Zhang, M.; Zhao, F.; Yang, Y.; An, T.; Qu, W.; Li, H.; Zhang, J.; Li, N. Catalytic Activity of Ferrates (NiFe₂O₄, ZnFe₂O₄ and CoFe₂O₄) on the Thermal Decomposition of Ammonium Perchlorate. *Propellants Explos. Pyrotech.* **2020**, *45*, 463–471. [[CrossRef](#)]
80. Liu, D.; Lu, Y.; Tan, H.-Q.; Chen, W.L.; Zhang, Z.M.; Li, Y.G.; Wang, E.B. Polyoxometalate-based purely inorganic porous frameworks with selective adsorption and oxidative catalysis functionalities. *Chem. Commun.* **2013**, *49*, 3673–3675. [[CrossRef](#)] [[PubMed](#)]
81. Wang, X.; Zhang, Q.; Zhang, Y.; Chen, H. Preparation of Ce doped NiFe₂O₄ nanoparticles and its catalysis on thermal decomposition of AP. *J. Solid Rocket Technol.* **2012**, *35*, 504–507.
82. Huang, R.C.; Chiu, W.J.; Lai, I.P.J.; Huang, C.C. Multivalent Aptamer/Gold Nanoparticle-Modified Graphene Oxide for Mass Spectrometry-Based Tumor Tissue Imaging. *Sci. Rep.* **2015**, *5*, 10292. [[CrossRef](#)] [[PubMed](#)]
83. Novoselov, K.S.; Geim, A.K.; Morozov, S.V.; Jiang, D.; Zhang, Y.; Dubonos, S.V.; Grigorieva, I.V.; Firsov, A.A. Electric field effect in atomically thin carbon films. *Science* **2004**, *306*, 666–669. [[CrossRef](#)]
84. Stoller, M.D.; Park, S.J.; Zhu, Y.W.; An, J.H.; Ruoff, R.S. Graphene-Based Ultracapacitors. *Nano Lett.* **2008**, *8*, 3498–3502. [[CrossRef](#)]
85. Ambrosi, A.; Pumera, M. Electrochemically Exfoliated Graphene and Graphene Oxide for Energy Storage and Electrochemistry Applications. *Chem. A Eur. J.* **2016**, *22*, 153–159. [[CrossRef](#)]
86. Lin, T.W.; Wu, H.Y.; Tasi, T.T.; Lai, Y.H.; Shen, H.H. Surface-enhanced Raman spectroscopy for DNA detection by the self-assembly of Ag nanoparticles onto Ag nanoparticle-graphene oxide nanocomposites. *Phys. Chem. Chem. Phys.* **2015**, *17*, 18443–18448. [[CrossRef](#)]
87. Haghghi, N.; Hallaj, R.; Salimi, A. Immobilization of glucose oxidase onto a novel platform based on modified TiO₂ and graphene oxide, direct electrochemistry, catalytic and photocatalytic activity. *Mater. Sci. Eng. C Mater. Biol. Appl.* **2017**, *73*, 417–424. [[CrossRef](#)] [[PubMed](#)]
88. Wu, Q.C.; Yu, R.; Zhou, Z.H.; Liu, H.W.; Jiang, R.L. Encapsulation of a Core-Shell Porous Fe₃O₄@Carbon Material with Reduced Graphene Oxide for Li⁺ Battery Anodes with Long Cyclability. *Langmuir* **2021**, *37*, 785–792. [[CrossRef](#)] [[PubMed](#)]
89. Wang, Y.Y.; Wang, Y.; Lu, L.G.; Zhang, B.; Wang, C.X.; He, B.; Wei, R.; Xu, D.D.; Hao, Q.L.; Liu, B. Hierarchically Hollow and Porous NiO/NiCo₂O₄ Nanoprisms Encapsulated in Graphene Oxide for Lithium Storage. *Langmuir* **2020**, *36*, 9668–9674. [[CrossRef](#)] [[PubMed](#)]
90. Wu, Y.S.; Yu, H.; Wang, H.J.; Peng, F. Controllable synthesis and catalytic performance of graphene-supported metal oxide nanoparticles. *Chin. J. Catal.* **2014**, *35*, 952–959. [[CrossRef](#)]
91. Ding, X.; Huang, Z.H.; Shen, W.C.; Kang, F.Y. Preparation and electrochemical performance of a CuO/graphene composite. *New Carbon Mater.* **2013**, *28*, 172–177. [[CrossRef](#)]
92. Danish, M.; Athar, M.S.; Ahmad, I.; Warshagha, M.Z.A.; Rasool, Z.; Muneer, M. Highly efficient and stable Fe₂O₃/g-C₃N₄/GO nanocomposite with Z-scheme electron transfer pathway: Role of photocatalytic activity and adsorption isotherm of organic pollutants in wastewater. *Appl. Surf. Sci.* **2022**, *604*, 154604. [[CrossRef](#)]
93. Kumar, R.; del Pino, A.P.; Sahoo, S.; Singh, R.K.; Tan, W.K.; Kar, K.K.; Matsuda, A.; Joanni, E. Laser processing of graphene and related materials for energy storage: State of the art and future prospects. *Prog. Energy Combust. Sci.* **2022**, *91*, 100981. [[CrossRef](#)]

94. Sharif, H.M.A.; Asif, M.B.; Wang, Y.; Hou, Y.-N.; Yang, B.; Xiao, X.; Li, C. Spontaneous intra-electron transfer within rGO@Fe₂O₃-MnO catalyst promotes long-term NO_x reduction at ambient conditions. *J. Hazard. Mater.* **2023**, *441*, 129951. [[CrossRef](#)]
95. Li, Z.M.; Wang, Y.; Zhang, Y.Q.; Liu, L.; Zhang, S.J. CL-20 hosted in graphene foam as a high energy material with low sensitivity. *RSC Adv.* **2015**, *5*, 98925–98928. [[CrossRef](#)]
96. Smeu, M.; Zahid, F.; Ji, W.; Guo, H.; Jaidann, M.; Abou-Rachid, H. Energetic Molecules Encapsulated Inside Carbon Nanotubes and between Graphene Layers: DFT Calculations. *J. Phys. Chem. C* **2011**, *115*, 10985–10989. [[CrossRef](#)]
97. Qin, M.; Zheng, X.; Tang, W.; Zhang, Y.; Shi, Q.; Qiu, S. Preparation and catalytic performance of Fe₂O₃/graphene composite. *J. Solid Rocket Technol.* **2017**, *40*, 601–604.
98. Zhang, T.; Li, C.C.; Wang, W.; Guo, Z.Q.; Pang, A.M.; Ma, H.X. Construction of Three-Dimensional Hematite/Graphene with Effective Catalytic Activity for the Thermal Decomposition of CL-20. *Acta Phys. Chim. Sin.* **2020**, *36*, 1905048.
99. Pei, J.Y.; Zhao, H.Y.; Yang, F.; Yan, D. Graphene Oxide/Fe₂O₃ Nanocomposite as an Efficient Catalyst for Thermal Decomposition of Ammonium Perchlorate via the Vacuum-Freeze-Drying Method. *Langmuir* **2021**, *37*, 6132–6138. [[CrossRef](#)] [[PubMed](#)]
100. Fertassi, M.A.; Liu, Q.; Li, R.Z.; Liu, P.G.; Liu, J.Y.; Chen, R.R.; Liu, L.H.; Wang, J. Ex situ synthesis of G/α-Fe₂O₃ nanocomposite and its catalytic effect on the thermal decomposition of ammonium perchlorate. *Bull. Mater. Sci.* **2017**, *40*, 691–698. [[CrossRef](#)]
101. Zhang, M.; Zhao, F.Q.; Yang, Y.J.; Zhang, J.K.; Li, N.; Gao, H.X. Effect of rGO-Fe₂O₃ nanocomposites fabricated in different solvents on the thermal decomposition properties of ammonium perchlorate. *Crystengcomm* **2018**, *20*, 7010–7019. [[CrossRef](#)]
102. Paredes, J.I.; Villar-Rodil, S.; Martinez-Alonso, A.; Tascon, J.M.D. Graphene oxide dispersions in organic solvents. *Langmuir* **2008**, *24*, 10560–10564. [[CrossRef](#)] [[PubMed](#)]
103. Villar-Rodil, S.; Paredes, J.I.; Martinez-Alonso, A.; Tascon, J.M.D. Preparation of graphene dispersions and graphene-polymer composites in organic media. *J. Mater. Chem.* **2009**, *19*, 3591–3593. [[CrossRef](#)]
104. Yan, N.; Qin, L.J.; Li, J.G.; Zhao, F.Q.; Feng, H. Atomic layer deposition of iron oxide on reduced graphene oxide and its catalytic activity in the thermal decomposition of ammonium perchlorate. *Appl. Surf. Sci.* **2018**, *451*, 155–161. [[CrossRef](#)]
105. Elbasuney, S.; El-Sayyad, G.S.; Yehia, M.; Aal, S.K.A. Facile synthesis of RGO-Fe₂O₃ nanocomposite: A novel catalyzing agent for composite propellants. *J. Mater. Sci. Mater. Electron.* **2020**, *31*, 20805–20815. [[CrossRef](#)]
106. Xu, X.; Wang, T.; Nie, K.; Jiang, X.; Jia, R. Preparation of BiFeO₃/rGO Nanocomposites and Its Catalytic Performance for the Thermal Decomposition of Ammonium Perchlorate. *Chin. J. Explos. Propellants* **2021**, *44*, 181–188.
107. Guo, Z.Q.; Qian, X.; Zhang, T.; Wang, Y.W.; Tao, B.W.; Li, L.; Ma, H.X.; Gu, J. Application of BiFeO₃/GO composite combustion catalyst in HTPB propellant. *J. Solid Rocket Technol.* **2022**, *45*, 61–66.
108. Chen, T.; Du, P.; Jiang, W.; Liu, J.; Hao, G.; Gao, H.; Xiao, L.; Ke, X.; Zhao, F.; Xuan, C. A facile one-pot solvothermal synthesis of CoFe₂O₄/RGO and its excellent catalytic activity on thermal decomposition of ammonium perchlorate. *RSC Adv.* **2016**, *6*, 83838–83847. [[CrossRef](#)]
109. Chen, T.; Jiang, W. A Facile Solvothermal Synthesis of NiFe₂O₄/RGO and Its Enhanced Catalytic Activity on Thermal Decomposition of Ammonium Perchlorate. In Proceedings of the 2017 IEEE 17th International Conference on Nanotechnology (IEEE-NANO), Pittsburgh, PA, USA, 25–28 July 2017; pp. 607–610.
110. Wang, W.; Guo, S.; Zhang, D.; Yang, Z. One-pot hydrothermal synthesis of reduced graphene oxide/zinc ferrite nanohybrids and its catalytic activity on the thermal decomposition of ammonium perchlorate. *J. Saudi Chem. Soc.* **2019**, *23*, 133–140. [[CrossRef](#)]
111. Iijima, S. Helical microtubules of graphitic carbon. *Nature* **1991**, *354*, 56–58. [[CrossRef](#)]
112. Li, W.Z.; Liang, C.H.; Qiu, J.S.; Zhou, W.J.; Han, H.M.; Wei, Z.B.; Sun, G.Q.; Xin, Q. Carbon nanotubes as support for cathode catalyst of a direct methanol fuel cell. *Carbon* **2002**, *40*, 791–794. [[CrossRef](#)]
113. Wang, J.N.; Li, X.D. Preparation of Ferric Oxide/Carbon Nanotubes Composite Nano-Particles and Catalysis on Burning Rate of Ammonium Perchlorate. *Chin. J. Explos. Propellants* **2006**, *29*, 44–47.
114. Jiang, W.; Liu, J.X.; Liu, Y.; Cui, P.; Li, F.S. Preparation of Fe₂O₃/CNTs composites and its catalysis on thermal decomposition of AP. *J. Solid Rocket Technol.* **2008**, *31*, 65–68.
115. Cui, Q.Z.; Jiao, J.Q.; Zhao, W.D. Preparation of Fe₂O₃/CNTs and Its Catalytic Mechanism on Thermal Decomposition of RDX. *Chin. J. Explos. Propellants* **2009**, *32*, 68–71.
116. Groenewolt, M.; Antonietti, M. Synthesis of g-C₃N₄ nanoparticles in mesoporous silica host matrices. *Adv. Mater.* **2005**, *17*, 1789–1792. [[CrossRef](#)]
117. Ghane, N.; Sadrezaad, S.K.; Hosseini, H.S.M. Combustion synthesis of g-C₃N₄/Fe₂O₃ nanocomposite for superior photoelectrochemical catalytic performance. *Appl. Surf. Sci.* **2020**, *534*, 147563. [[CrossRef](#)]
118. Yan, S.D.; Shi, Y.; Tao, Y.F.; Zhang, H. Enhanced persulfate-mediated photocatalytic oxidation of bisphenol A using bioelectricity and a g-C₃N₄/Fe₂O₃ heterojunction. *Chem. Eng. J.* **2019**, *359*, 933–943. [[CrossRef](#)]
119. Lian, X.; Xue, W.; Dong, S.; Liu, E.; Li, H.; Xu, K. Construction of S-scheme Bi₂WO₆/g-C₃N₄ heterostructure nanosheets with enhanced visible-light photocatalytic degradation for ammonium dinitramide. *J. Hazard. Mater.* **2021**, *412*, 125217. [[CrossRef](#)] [[PubMed](#)]
120. Li, Q.; He, Y.; Peng, R.F. Graphitic carbon nitride (g-C₃N₄) as a metal-free catalyst for thermal decomposition of ammonium perchlorate. *RSC Adv.* **2015**, *5*, 24507–24512. [[CrossRef](#)]
121. Wang, R.H.; Song, W.K.; Guo, C.P.; Gong, W.; Wang, D.J. Characterization of g-C₃N₄/Fe₂O₃ Composite Catalyst and Its Catalytic Effect on Ammonium Perchlorate. *J. Propuls. Technol.* **2022**, *43*, 373–378.

122. Wan, C.; Wang, C.; Chen, S.H.; Xu, K.Z. Catalytic Decomposition Properties of $\text{CoFe}_2\text{O}_4/\text{g-C}_3\text{N}_4$ on HMX and TKX-50. *Chin. J. Energetic Mater.* **2022**, *30*, 703–709.
123. Wang, J.; Lian, X.; Chen, S.; Li, H.; Xu, K. Effect of $\text{Bi}_2\text{WO}_6/\text{g-C}_3\text{N}_4$ composite on the combustion and catalytic decomposition of energetic materials: An efficient catalyst with $\text{g-C}_3\text{N}_4$ carrier. *J. Colloid Interface Sci.* **2022**, *610*, 842–853. [[CrossRef](#)]
124. An, T.; Zhao, F.Q.; Pei, Q.; Xiao, L.B.; Xu, S.Y.; Gao, H.X.; Xing, X.L. Preparation, Characterization and Combustion Catalytic Activity of Nanoparticle Super Thermites. *Chin. J. Inorg. Chem.* **2011**, *27*, 231–238.
125. An, T.; Zhao, F.Q.; Yi, J.H.; Fan, X.Z.; Gao, H.X.; Hao, H.X.; Wang, X.H.; Hu, R.Z.; Pei, Q. Preparation, Characterization, Decomposition Mechanism and Non-Isothermal Decomposition Reaction Kinetics of the Super Thermite Al/CuO Precursor. *Acta Phys. Chim. Sin.* **2011**, *27*, 281–288.
126. Xu, H.; Li, X.; Zhao, F.; Pang, W.; Jia, S.; Mo, H. Review on Application of Nano-metal Powders in Explosive and Propellants. *Energetic Mater.* **2011**, *19*, 232–239.
127. Pang, W.Q.; Fan, X.Z.; Lv, K. Physicochemical properties of boron powder and its application in fuel-rich solid propellants. *Aerodyn. Missile J.* **2009**, *10*, 53–58.
128. Pei, J.; Zhao, F.; Song, X.; Zheng, W. Research Progress in the Application of Lightweight Carbon Materials and Their Composites in Solid Rocket Propellants. *Chin. J. Explos. Propellants* **2014**, *37*, 1–6.
129. Puszynski, J.A.; Bulian, C.J.; Swiatkiewicz, J.J. Processing and ignition characteristics of aluminum-bismuth trioxide nanothermite system. *J. Propuls. Power* **2007**, *23*, 698–706. [[CrossRef](#)]
130. Qi, Q.F.; Zhang, X.H.; Yan, Q.L.; Song, Z.W.; Liu, P.; Li, J.Z. Research progress on the application of nano-metals and their composites in solid propellants. *Chem. Propellants Polym. Mater.* **2012**, *10*, 66–72.
131. Bhattacharya, S.; Gao, Y.F.; Apperson, S.; Subramaniam, S.; Shende, R.; Gangopadhyay, S.; Talantsev, E. A novel on-chip diagnostic method to measure burn rates of energetic materials. *J. Energetic Mater.* **2006**, *24*, 1–15. [[CrossRef](#)]
132. Nie, H.Q.; Chan, H.Y.; Pisharath, S.; Hng, H.H. Combustion characteristic and aging behavior of bimetal thermitic powders. *Def. Technol.* **2021**, *17*, 755–762. [[CrossRef](#)]
133. Shen, L.H.; Li, G.P.; Luo, Y.J.; Gao, K.; Ge, Z. Preparation and characterization of $\text{Al}/\text{B}/\text{Fe}_2\text{O}_3$ nanothermites. *Sci. China Chem.* **2014**, *57*, 797–802. [[CrossRef](#)]
134. Zhang, T.; Li, J.C.; Qin, Z.; Li, C.C.; Gao, H.X.; Zhao, F.Q.; Ma, H.X. Doping hematite with bismuth to enhance its catalytic and oxidizing properties. *Chem. Eng. J.* **2021**, *421*, 129436. [[CrossRef](#)]
135. Yan, N.; Qin, L.J.; Hao, H.X.; Hui, L.F.; Zhao, F.Q.; Feng, H. Iron oxide/aluminum/graphene energetic nanocomposites synthesized by atomic layer deposition: Enhanced energy release and reduced electrostatic ignition hazard. *Appl. Surf. Sci.* **2017**, *408*, 51–59. [[CrossRef](#)]
136. Malchi, J.Y.; Foley, T.J.; Yetter, R.A. Electrostatically Self-Assembled Nanocomposite Reactive Microspheres. *Acs Appl. Mater. Interfaces* **2009**, *1*, 2420–2423. [[CrossRef](#)] [[PubMed](#)]
137. Kuntz, J.D.; Cervantes, O.G.; Gash, A.E.; Munir, Z.A. Tantalum-tungsten oxide thermitic composites prepared by sol-gel synthesis and spark plasma sintering. *Combust. Flame* **2010**, *157*, 1566–1571. [[CrossRef](#)]
138. Ke, X.; Zhou, X.; Hao, G.Z.; Xiao, L.; Liu, J.; Jiang, W. Rapid fabrication of superhydrophobic $\text{Al}/\text{Fe}_2\text{O}_3$ nanothermite film with excellent energy-release characteristics and long-term storage stability. *Appl. Surf. Sci.* **2017**, *407*, 137–144. [[CrossRef](#)]
139. He, W.; Tao, B.W.; Yang, Z.J.; Yang, G.C.; Guo, X.; Liu, P.J.; Yan, Q.L. Mussel-inspired polydopamine-directed crystal growth of core-shell n-Al@PDA@CuO metastable intermixed composites. *Chem. Eng. J.* **2019**, *369*, 1093–1101. [[CrossRef](#)]
140. He, W.; Liu, P.J.; He, G.Q.; Gozin, M.; Yan, Q.L. Highly Reactive Metastable Intermixed Composites (MICs): Preparation and Characterization. *Adv. Mater.* **2018**, *30*, 1706293. [[CrossRef](#)] [[PubMed](#)]
141. Shen, J.P.; Qiao, Z.Q.; Wang, J.; Yang, G.C.; Chen, J.; Li, Z.Q.; Liao, X.; Wang, H.Y.; Zachariah, M.R. Reaction mechanism of Al-CuO nanothermites with addition of multilayer graphene. *Thermochim. Acta* **2018**, *666*, 60–65. [[CrossRef](#)]
142. Wang, A.Q.; Bok, S.; Thiruvengadathan, R.; Gangopadhyay, K.; McFarland, J.A.; Maschmann, M.R.; Gangopadhyay, S. Reactive nanoenergetic graphene aerogel synthesized by one-step chemical reduction. *Combust. Flame* **2018**, *196*, 400–406. [[CrossRef](#)]
143. Zhao, W.J.; Ren, H.; Yan, T.; Ou, Y.P.; Jiao, Q.J.; Wang, H.Y.; Kline, D.J.; Zachariah, M.R. Tailoring energy release of nano-Si based thermites via incorporation of Ti nanoparticles. *Chem. Eng. J.* **2020**, *396*, 124559. [[CrossRef](#)]
144. Martirosyan, K.S. Nanoenergetic Gas-Generators: Principles and applications. *J. Mater. Chem.* **2011**, *21*, 9400–9405. [[CrossRef](#)]
145. Wu, T.; Lahiner, G.; Tenaillon, C.; Reig, B.; Hungria, T.; Esteve, A.; Rossi, C. Unexpected enhanced reactivity of aluminized nanothermites by accelerated aging. *Chem. Eng. J.* **2021**, *418*, 129432. [[CrossRef](#)]
146. Zakiyyan, N.; Wang, A.Q.; Thiruvengadathan, R.; Staley, C.; Mathai, J.; Gangopadhyay, K.; Maschmann, M.R.; Gangopadhyay, S. Combustion of aluminum nanoparticles and exfoliated 2D molybdenum trioxide composites. *Combust. Flame* **2018**, *187*, 1–10. [[CrossRef](#)]
147. Wang, W.M.; Liu, B.; Xu, K.Z.; Zu, Y.Q.; Song, J.R.; Zhao, F.Q. In-situ preparation of $\text{MgFe}_2\text{O}_4\text{-GO}$ nanocomposite and its enhanced catalytic reactivity on decomposition of AP and RDX. *Ceram. Int.* **2018**, *44*, 19016–19020. [[CrossRef](#)]
148. Yan, Q.L.; Zhao, F.Q.; Kuo, K.K.; Zhang, X.H.; Zeman, S.; DeLuca, L.T. Catalytic effects of nano additives on decomposition and combustion of RDX-, HMX-, and AP-based energetic compositions. *Prog. Energy Combust. Sci.* **2016**, *57*, 75–136. [[CrossRef](#)]
149. Wang, W.M.; Li, H.; Zhang, M.; Zhao, F.Q.; Xu, S.Y.; Wang, C.J.; Qin, Z.; An, T.; Xu, K.Z. Effects of oxidizer and architecture on the thermochemical reactivity, laser ignition and combustion properties of nanothermite. *Fuel* **2022**, *314*, 123141. [[CrossRef](#)]

150. Shi, L.M.; Zhang, W.C.; Cheng, J.; Yu, C.P.; Shen, R.Q.; Ye, J.H.; Qin, Z.C.; Chao, Y.M. A high energy output and low onset temperature nanothermite based on three-dimensional ordered macroporous nano-NiFe₂O₄. *RSC Adv.* **2016**, *6*, 93330–93334. [[CrossRef](#)]
151. Yang, H.T.; Liu, Y.F.; Huang, H.T.; Zhao, Y.; Song, K.G.; Wang, H.Y.; Xie, W.X.; Cheng, Y.; Fan, X.Z. Preparation and characterization of the Al/Fe₂O₃/RDX/NC nanocomposites by electrospray. *J. Therm. Anal. Calorim.* **2019**, *137*, 1615–1620. [[CrossRef](#)]
152. Gao, K.; Li, G.P.; Luo, Y.J.; Wang, L.; Shen, L.H.; Wang, G. Preparation and characterization of the AP/Al/Fe₂O₃ ternary nano-thermites. *J. Therm. Anal. Calorim.* **2014**, *118*, 43–49. [[CrossRef](#)]
153. Zhao, N.N.; He, C.C.; Liu, J.B.; Ma, H.X.; An, T.; Zhao, F.Q.; Hu, R.Z. Preparation and Characterization of Superthermite Al/Fe₂O₃ and Its Effect on Thermal Decomposition of Cyclotrimethylene Trinitramine. *Acta Phys. Chim. Sin.* **2013**, *29*, 2498–2504.
154. Zhang, T.; Zhao, N.; Li, J.; Gong, H.; An, T.; Zhao, F.; Ma, H. Thermal behavior of nitrocellulose-based superthermites: Effects of nano-Fe₂O₃ with three morphologies. *RSC Adv.* **2017**, *7*, 23583–23590. [[CrossRef](#)]
155. Zhong, L.; Zhou, X.; Huang, X.Y.; Zheng, D.W.; Mao, Y.F.; Wang, R.H.; Wang, D.J. Combustion/decomposition characteristics of 3D-printed Al/CuO, Al/Fe₂O₃, Al/Bi₂O₃ and Al/PTFE hollow filaments. *Mater. Chem. Phys.* **2021**, *271*, 124874. [[CrossRef](#)]
156. Kabra, S.; Gharde, S.; Gore, P.M.; Jain, S.; Khire, V.H.; Kandasubramanian, B. Recent trends in nanothermites: Fabrication, characteristics and applications. *Nano Express* **2020**, *1*, 032001. [[CrossRef](#)]

Disclaimer/Publisher’s Note: The statements, opinions and data contained in all publications are solely those of the individual author(s) and contributor(s) and not of MDPI and/or the editor(s). MDPI and/or the editor(s) disclaim responsibility for any injury to people or property resulting from any ideas, methods, instructions or products referred to in the content.